

2006

# Adaptive resonant mode control for high frequency tonal noise

Tom Waite  
*Iowa State University*

Follow this and additional works at: <https://lib.dr.iastate.edu/rtd>

 Part of the [Electrical and Electronics Commons](#), and the [Mechanical Engineering Commons](#)

## Recommended Citation

Waite, Tom, "Adaptive resonant mode control for high frequency tonal noise " (2006). *Retrospective Theses and Dissertations*. 1373.  
<https://lib.dr.iastate.edu/rtd/1373>

This Thesis is brought to you for free and open access by the Iowa State University Capstones, Theses and Dissertations at Iowa State University Digital Repository. It has been accepted for inclusion in Retrospective Theses and Dissertations by an authorized administrator of Iowa State University Digital Repository. For more information, please contact [digirep@iastate.edu](mailto:digirep@iastate.edu).

**Adaptive resonant mode control for high frequency tonal noise**

by

Tom Waite

A thesis submitted to the graduate faculty  
in partial fulfillment of the requirements for the degree of  
MASTER OF SCIENCE

Major: Mechanical Engineering

Program of Study Committee:  
Atul G. Kelkar, Major Professor  
J. Adin Mann III  
Jerald M. Vogel

Iowa State University

Ames, Iowa

2006

Copyright © Tom Waite, 2006. All rights reserved.

UMI Number: 1439836



---

UMI Microform 1439836

Copyright 2007 by ProQuest Information and Learning Company.  
All rights reserved. This microform edition is protected against  
unauthorized copying under Title 17, United States Code.

---

ProQuest Information and Learning Company  
300 North Zeeb Road  
P.O. Box 1346  
Ann Arbor, MI 48106-1346

## TABLE OF CONTENTS

<b>LIST OF TABLES</b> . . . . .	iv
<b>LIST OF FIGURES</b> . . . . .	v
<b>ACKNOWLEDGEMENTS</b> . . . . .	viii
<b>CHAPTER 1. Introduction</b> . . . . .	1
1.1 Outline . . . . .	2
1.2 Remarks . . . . .	3
<b>CHAPTER 2. System Identification</b> . . . . .	4
2.1 Enhancements to SOCIT Algorithms . . . . .	6
2.2 Modulating the Model . . . . .	12
2.3 Remarks . . . . .	18
<b>CHAPTER 3. Synthesis of State Weights</b> . . . . .	20
3.1 Problem Description . . . . .	21
3.2 Control Design . . . . .	22
3.2.1 State Weighting Using Trial and Error Approach . . . . .	24
3.2.2 Automated State Weighting . . . . .	27
3.3 Remarks . . . . .	32
<b>CHAPTER 4. In-Seat Active Noise Control</b> . . . . .	33
4.1 Broadband Control . . . . .	34
4.2 Resonant Mode Control . . . . .	39

4.2.1	Controller Design . . . . .	40
4.2.2	Controller Performance . . . . .	42
4.3	Remarks . . . . .	46
<b>CHAPTER 5. Adaptive Resonant Mode Control . . . . .</b>		<b>47</b>
5.1	Experimental Setup . . . . .	48
5.2	Control Design . . . . .	49
5.3	Adaptive Design . . . . .	55
5.3.1	Implementation . . . . .	56
5.3.2	Results . . . . .	59
5.4	Remarks . . . . .	61
<b>CHAPTER 6. Feedforward Control . . . . .</b>		<b>64</b>
6.1	Band-Limited Plant Inversion . . . . .	64
6.2	Preview-Based Cancellation . . . . .	68
6.3	Remarks . . . . .	69
<b>CHAPTER 7. Conclusions and Future Work . . . . .</b>		<b>72</b>
<b>BIBLIOGRAPHY . . . . .</b>		<b>74</b>

**LIST OF TABLES**

Table 3.1	Comparison of the two methods. . . . .	32
Table 5.1	Trade-off showing the adaptation update rate and the resolution for determining the center frequency of the notch ( $f_s = 65536$ Hz). 61	

## LIST OF FIGURES

Figure 2.1	Best model obtained using Matlab's Invfreqs program. Converting the transfer function to state-space form will ruin the accuracy of the model. . . . .	5
Figure 2.2	Undersampled discrete to continuous-time system conversions cause distortions in the model. . . . .	7
Figure 2.3	Correction of distortions caused by undersampled discrete to continuous-time system conversion using the prewarp method. . . . .	10
Figure 2.4	Error grid showing how changes in the sampling rate ratio ( $f_s$ /half the Nyquist rate) effects the accuracy of the resulting model. Blue: Small Error, Red: Large Error. . . . .	11
Figure 2.5	Error grid showing how changes in the gain shift of the experimental data effects the accuracy of the resulting model. Blue: Small Error, Red: Large Error. . . . .	13
Figure 2.6	Experimental Data (blue) is flipped and shifted to the origin where it is then prewarped (red) and modelled (green) using SOCIT. . . . .	14
Figure 2.7	Modulating the nth order system identified at the origin results in a model of order 2n centered around the carrier frequency. . .	17
Figure 2.8	Model accuracy is maintained even after deleting all states having frequency components larger than 400 Hz. . . . .	18

Figure 3.1	Section of airplane panel instrumented with four accelerometer sensors and one piezoelectric actuator. . . . .	22
Figure 3.2	Block diagram of closed loop system. . . . .	23
Figure 3.3	Simulation of controller reductions using state weights found by guessing and checking. . . . .	26
Figure 3.4	Simulation of controller reductions using state weights found by the automation method. . . . .	30
Figure 3.5	Energy and maximum amplitude reduction progressing over the first 50 seconds of iteration. . . . .	31
Figure 4.1	The active headrest experimental setup using a dummy head in an anechoic chamber. . . . .	35
Figure 4.2	40th order model shows a very flat magnitude response and a large phase delay over the entire frequency range. . . . .	36
Figure 4.3	Pole-zero mapping of the transfer function of the system reveals many right-half-plane zeros. . . . .	37
Figure 4.4	Only 1-2 dB of reduction achievable because of nearly flat free field dynamics and a large phase delay. . . . .	38
Figure 4.5	4th order controller and 2nd order reduced controller show almost no difference. . . . .	41
Figure 4.6	Resonant Mode Controller Block Diagram. . . . .	42
Figure 4.7	Simulation of white noise disturbance with controller on and off. . . . .	43
Figure 4.8	Error microphone must be positioned within 1 cm of the ear to achieve desired performance. . . . .	44
Figure 4.9	Simulation showing the 1 cm radius quiet regions possible with perfect cancellation at 6400 Hz. Quiet regions are in blue. Noise is increased in red regions. . . . .	45

Figure 5.1	Electret microphone amplifier circuit schematic. . . . .	49
Figure 5.2	Microphones and microphone filter/amplifier box. . . . .	50
Figure 5.3	Headset setup with feedback microphone (red wire) in the dummy ear and feedforward microphone (yellow wire) and speaker (white wire) just outside the ear. . . . .	51
Figure 5.4	Desired loop response of 6 dB gain margin and infinite phase margin. . . . .	55
Figure 5.5	Resonant controllers for the headset spanning the entire region of control. . . . .	57
Figure 5.6	Controller matrix elements as a function of frequency. . . . .	58
Figure 5.7	Simulation diagram of $H_{con}$ with adaptive state-space variables. . . . .	60
Figure 5.8	Frequency-varying primary tone shows 20 dB of reduction. . . . .	62
Figure 6.1	A nonrealizable filter is required for perfect feedforward control. . . . .	66
Figure 6.2	Feedforward control performance shows wide-band reductions as well as increases. . . . .	67
Figure 6.3	Required filter transfer functions for different disturbance positions. . . . .	68
Figure 6.4	Preview-based controller block diagram. . . . .	69
Figure 6.5	Preview-based feedforward performance with control input signal determined off-line. . . . .	70

## **ACKNOWLEDGEMENTS**

I would like to thank Dr. Atul Kelkar for his guidance and support throughout this project. I also want to thank Dr. Adin Mann and Dr. Jerald Vogel for serving on my program of study committee. This thesis is dedicated to my family.

## CHAPTER 1. Introduction

Active noise control has typically been relegated to low frequency noise due to challenging technical issues that arise when controlling high frequencies. These technical issues include a lack of modal separation in the plant response, a small region of control around the error microphone, large model uncertainty, and impractical physical configurations imposed on the sensor/actuator pair. This thesis explores a variety of these issues by examining various feedback and feedforward controllers using a couple of different experimental setups.

In noise-mitigating headset designs, passive noise control approaches have shown substantial broadband reductions of high frequency noise using well-sealed ear defenders lined with sound absorbing foam. These passive headsets could exhibit even further noise reduction with the addition of an active system. In some cases, people working in a noisy environment all day do not wear ear defenders as often times they can be uncomfortable to wear for long periods of time. An active headset system would allow these people to be free of an uncomfortable headset while reducing the risk of potential hearing loss. Also, passive headsets limit speech intelligibility, whereas active systems can selectively control bands of the frequency spectrum not conflicting with human speech. These are a few of the motivations behind the research presented in this thesis.

The main contribution of this thesis is the formulation of a new type of resonant mode controller for which a closed form expression is derived. This controller requires no design iterations and the gain margin of the resulting loop can be specified ahead of time (the phase margin is always infinite). This controller differs from standard resonant

control in that it acts directly on a disturbance rather than damping resonant poles of the system plant. This allows for a notch to be created in the disturbance anywhere in the spectrum and not just at resonant modes of the system. This becomes necessary when controlling high frequency noise in the free field where no resonant modes exist. Experimental results show large reductions ( $>20$  dB) can be achieved at high frequencies using this controller.

## 1.1 Outline

Chapter 2 examines the system identification software developed at NASA Langley Research Center, called SOCIT. Despite a few limitations, models obtained with this algorithm have a fairly good level of fidelity. The first of these limitations is that the accuracy of the identified discrete-time model increases as the sampling rate decreases. The model which best fits the data is therefore undersampled and warps significantly when converted to a continuous-time model. To solve this problem a method of pre-warping frequency response data is employed to obtain accurate continuous-time models. Another limitation of SOCIT is its inability to model high frequency data which does not begin at the origin. This problem is solved by introducing a concept known in communications as modulation.

Chapter 3 introduces a simple algorithm which automates the state weighting process required in LQG controller design. The standard method of trial and error until a desired performance is reached becomes increasingly more difficult and time consuming as the model order increases. The automated procedure is compared to the trial and error method using a 40th order system. It is shown that the algorithm is consistently able to find state weights which result in better performance in much less time than that taken by the trial and error method.

Chapter 4 investigates the configuration wherein an active noise control system is

mounted in a headrest. The non-separable modes in the plant response lead to a resonant control strategy which does not rely on damping resonant peaks of the plant. The implementation of the resulting controller design has a notch filter effect on a disturbance noise at any desired frequency. Unfortunately, the headrest setup shows a lack of robustness at high frequencies due to the large uncertainties caused by the speaker and microphone separation.

Chapter 5 attempts to remedy the lack of robustness of the headrest design with the use of a headset configuration. This setup involves the use of very small speakers and microphones to enable close proximity to the listener's ear. The closed form resonant mode controller equations are derived. An adaptive controller based on these equations is implemented which reduces a frequency varying disturbance.

Chapter 6 explores several possible feedforward control designs. It is determined that complete cancellation can only occur with the use of an unrealizable filter. A band-limited realizable filter design achieves satisfactory results, however it's lack of robustness to changes in the disturbance location limit it's feasibility. A preview-based feedforward controller is implemented off-line with promising results. Future work should address implementation of this methodology in real-time experiments.

## 1.2 Remarks

The first two chapters on system identification and automated state weighting essentially describe two computer codes which were developed to improve current modelling procedures and controller design. These chapters are not specific to the topic of resonant mode control and are generic to modelling and control design of any dynamic system. These two codes were extensively used in the resonant mode control designs presented in this thesis. For a demonstration of the capabilities of the above mentioned codes, some high order acoustic/vibration systems were used as examples.

## CHAPTER 2. System Identification

System identification is the process of extracting a mathematical model of a system using input/output data obtained experimentally. For a linear system, this mathematical model can be written in the form of a transfer function or as an equivalent state-space representation. This chapter focuses on system identification of an acoustical system to obtain a linear model. Often times for broadband acoustical systems it is more convenient and accurate to obtain a dynamic model using a system identification process rather than a mathematical derivation. Obtaining an accurate system model is key to controller robustness and performance.

3-D acoustics and vibrations problems with complex geometries are extremely difficult to solve analytically and their solutions tend to be an inaccurate representation of the actual system. On the other hand, obtaining a frequency response experimentally is not very difficult, a process made even simpler with the use of a dual-channel spectrum analyzer. Once the data has been collected, system identification programs must be used to fit a proper model to the data. In the case of acoustics and vibrations systems, frequency domain techniques tend to yield better fits to the model than the time domain methods and hence frequency domain system identification techniques are used in this work.

Matlab has a built-in command for frequency domain system identification called *invfreqs* which uses least squares error minimization to fit the data. The *invfreqs* function operates under the transfer function framework, so its output is the numerator and denominator coefficients of the modelled system's transfer function. This method is not

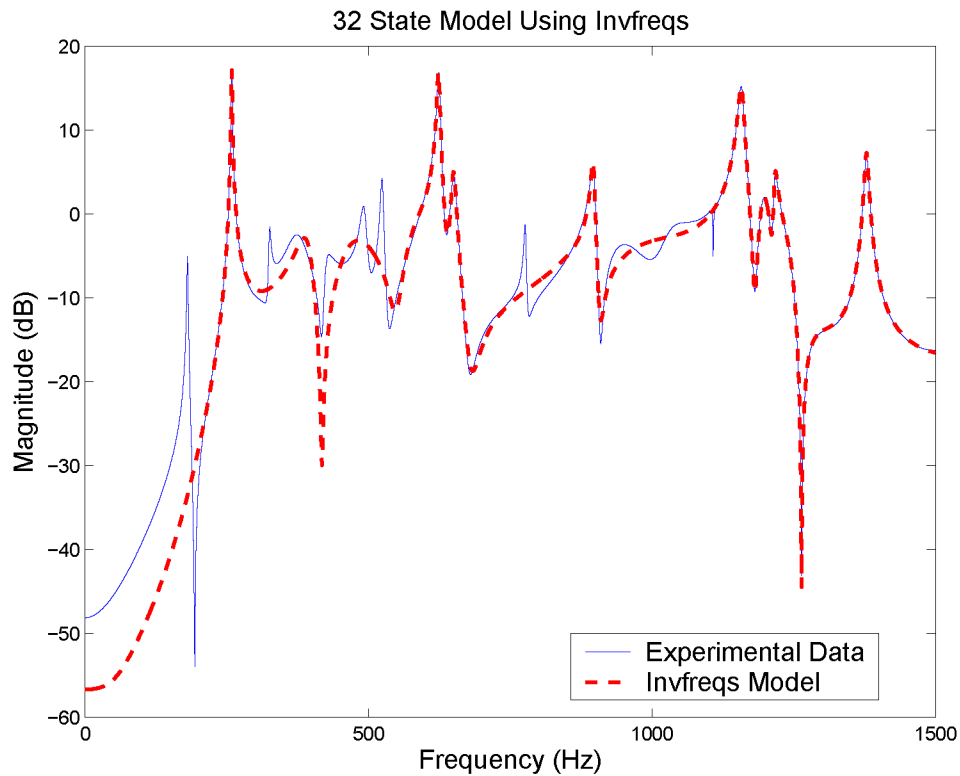


Figure 2.1 Best model obtained using Matlab's *Invfreqs* program. Converting the transfer function to state-space form will ruin the accuracy of the model.

well-suited for acoustics/vibrations systems because converting to modal canonical form ruins the accuracy of the model. This is because the model that *invfreqs* outputs is very ill-conditioned, even for low order systems. In addition, *invfreqs* is slow and degrades in accuracy for high order models (40th order and higher). A plot showing the best model *invfreqs* was able to achieve using the data from an aircraft panel vibration response is shown in Fig. 2.1.

Another frequency domain system identification routine is SOCIT (System Observer Controller Identification Toolbox) developed at NASA Langley Research Center. SOCIT makes use of the eigensystem realization algorithm to compute a discrete-time model from experimental magnitude and phase data using samples of the pulse response of the system (Markov parameters) (8). This program is well-suited for acoustics and vibrations

problems because it outputs a model in state-space form which is well-conditioned and easily converts to modal canonical form. It is also able to identify very high order plant dynamics with acceptable error levels fairly efficiently. Unfortunately, there are two major drawbacks of the SOCIT algorithm:

1. SOCIT's accuracy deteriorates as the model's chosen sampling rate increases. Therefore, the discrete-time models which SOCIT identifies are most accurate when sampled at the Nyquist rate (twice the highest frequency of the experimental data). This turns out to be a severe limitation when converting to a continuous-time model. Since the sampling rate is so low, the discrete-time model becomes distorted when it is transformed to a continuous-time system.
2. SOCIT is unable to find an accurate model of frequency response data at any location other than the origin. If the data is not given from 0 Hz to half of the Nyquist frequency, SOCIT will identify spurious modes of the system at points throughout this range anyway. These spurious modes cause the model order to be unnecessarily high and even after order reduction the identified model does not match up well with the experimental data.

These two restrictions prove to be limiting to an impractical level. The following two sections will outline how to obtain an undistorted continuous-time system from an undersampled discrete-time system and how to obtain an accurate model at any frequency range of interest. The resulting system identification procedure is a modification of the SOCIT toolbox which achieves extremely accurate frequency domain system models.

## **2.1 Enhancements to SOCIT Algorithms**

Frequency response data was gathered from a spectrum analyzer to identify the piezo-input accelerometer-output transfer function of a vibrating panel from 0 Hz to 1500 Hz.

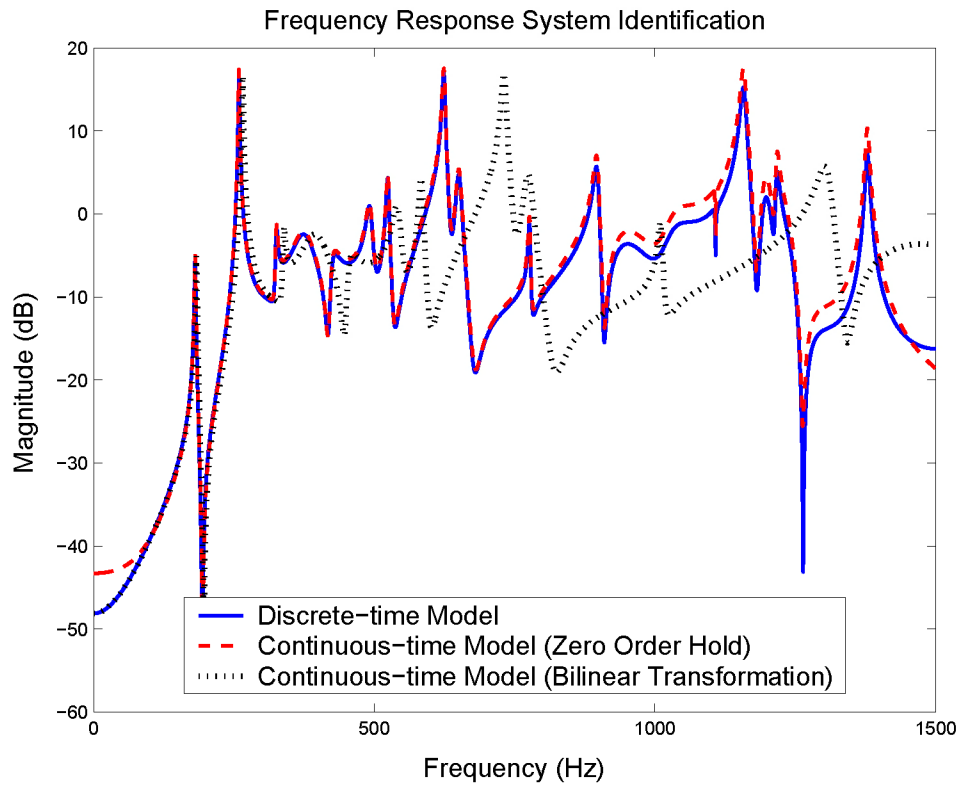


Figure 2.2 Undersampled discrete to continuous-time system conversions cause distortions in the model.

SOCIT was used to transform this frequency response data into a discrete-time state space representation with a sampling rate of 3000 Hz. As expected, the discrete to continuous conversion resulted in a distorted frequency response regardless of what type of transformation was used. Both conversion processes require the sampling rate to be much higher than the Nyquist rate for the dynamics to remain intact. The discrete-time model, as well as the continuous-time models obtained from the two conversion processes are shown in Fig. 2.2.

The zero order hold method, governed by Eq. (2.1), shows that the dynamics of the sample and hold are multiplied to the discrete-time system,  $G(z)$ , and then inverse  $Z$ -transformed to obtain the continuous-time system,  $G(s)$  (14). This means that it is impossible to predict how the conversion will warp discrete-time systems in general since

the amount of warping depends on the system itself.

$$G(s) = s\mathbf{Z}^{-1}\left\{\left(\frac{z}{z-1}\right)G(z)\right\} \quad (2.1)$$

Although the continuous-time model obtained using the bilinear transformation is much more distorted than the zero order hold model (see Fig. 2.2), it will be shown that the distortion can be predicted for any discrete-time system. The bilinear transformation maps the unit circle of the  $z$ -plane directly onto the imaginary axis of the  $s$ -plane according to Eq. (2.2)(14). What follows is the development of this equation into the actual frequency mapping from discrete-time system frequencies,  $f_d$ , to continuous-time system frequencies,  $f_c$ , given in Eq. (2.3)(10). This function predicts exactly how the discrete-time system will be warped into its continuous-time counterpart by a nonlinear frequency stretching. Since this relation depends only on the sampling rate,  $f_s$ , the amount of warping can be predicted for any discrete-time system. To obtain a continuous-time system which will match the transfer function data, the actual data must be prewarped according to Eq. (2.4), which is simply Eq. (2.3) solved for  $f_d$ . Therefore, to obtain an accurate continuous-time model, the user must shrink the actual data's frequency vector,  $\vec{f}$ , into a prewarped frequency vector,  $\vec{f}_p$ , before performing system identification.

$$s = 2f_s \left( \frac{z-1}{z+1} \right) \quad (2.2)$$

$$j2\pi f_c = 2f_s \left( \frac{z-1}{z+1} \right) \Big|_{z=e^{j2\pi f_d/f_s}}$$

$$= 2f_s \left( \frac{e^{j2\pi f_d/f_s} - 1}{e^{j2\pi f_d/f_s} + 1} \right)$$

$$= 2f_s \left( \frac{e^{j\pi f_d/f_s} - e^{-j\pi f_d/f_s}}{e^{j\pi f_d/f_s} + e^{-j\pi f_d/f_s}} \right)$$

$$= j2f_s \tan\left(\frac{\pi f_d}{f_s}\right)$$

$$f_c = \left(\frac{f_s}{\pi}\right) \tan\left(\frac{\pi f_d}{f_s}\right) \quad (2.3)$$

$$\vec{f}_p = \left(\frac{f_s}{\pi}\right) \tan^{-1}\left(\frac{\pi \vec{f}}{f_s}\right) \quad (2.4)$$

The SOCIT toolbox will fit a discrete-time model to the prewarped data so that when the model is converted to continuous-time, the requisite warping will stretch the discrete-time model directly on top of the experimental transfer function data. This system identification process, as applied to the aircraft panel dynamics, is shown in Fig. 2.3. The 40 state continuous-time system obtained from this modified SOCIT frequency domain identification procedure has extremely small error when compared with the experimental frequency response data.

There are several parameters involved in this procedure which are key to finding good models. One of these parameters is  $f_s$  from Eq. (2.4). Since the data is now being prewarped, a sampling frequency at the Nyquist rate is no longer required. In fact, since the output of the modified SOCIT program is a continuous-time model, the sampling rate can be just about anything (even below the Nyquist frequency). The size of  $f_s$  will only determine how much the data shrinks as a discrete-time model before it is stretched back out again by the discrete-to-continuous conversion. A small  $f_s$  results in a large amount of shrinking and stretching, whereas a large  $f_s$  will barely alter the experimental data. In order to determine a good value of  $f_s$ , a search over a grid of varying  $f_s$  ratios ( $f_s$ /half the Nyquist rate) and varying desired number of states was completed. The error between the resulting model and the experimental data was evaluated at each grid point and is plotted as a colormap in Fig. 2.4. As can be seen in the figure, an  $f_s$  ratio of 2 seems to be optimal since it required the fewest states to accomplish minimal error.

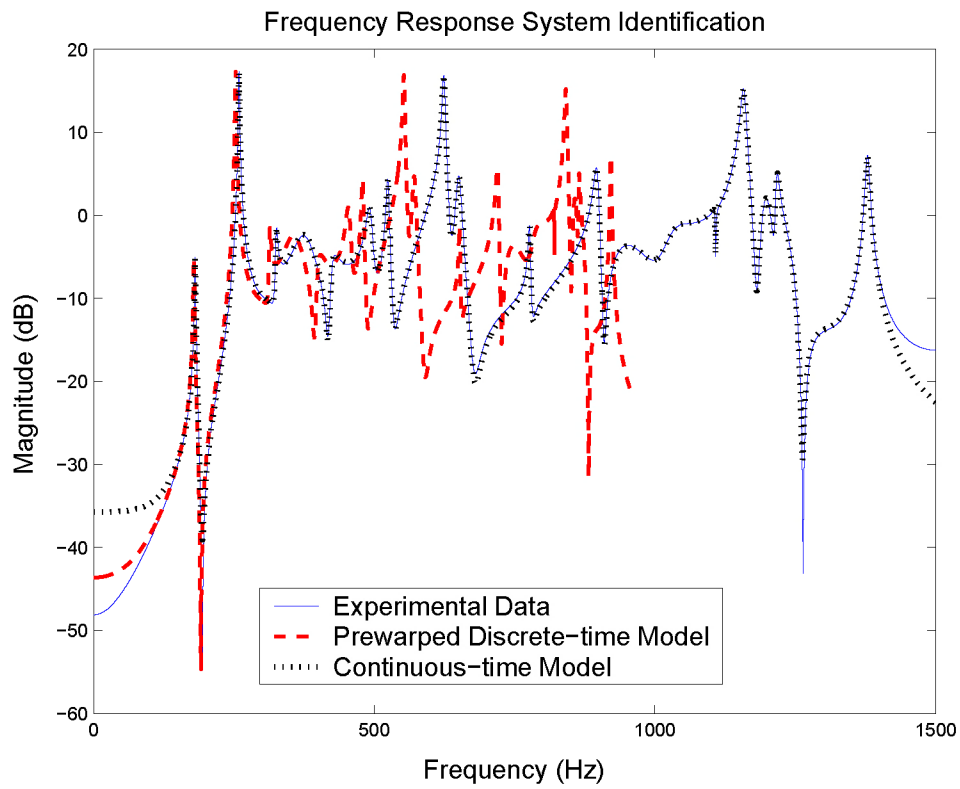


Figure 2.3 Correction of distortions caused by undersampled discrete to continuous-time system conversion using the prewarp method.

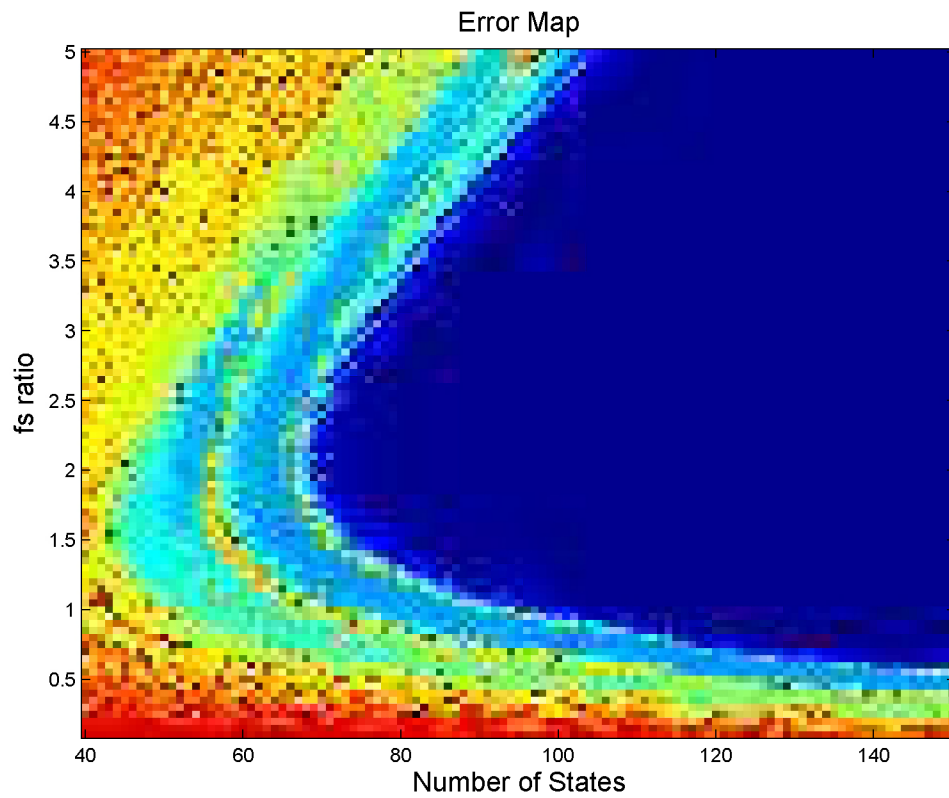


Figure 2.4 Error grid showing how changes in the sampling rate ratio ( $f_s$ /half the Nyquist rate) effects the accuracy of the resulting model. Blue: Small Error, Red: Large Error.

Another important parameter involved in fitting an accurate model comes from the gain-scaling factor. This is given as an amplitude shift in dB of the experimental data before sending it as input into SOCIT's identification routine. This conditioning of the input data can lead to better models than doing no scaling at all. This is especially true for high order systems where the model error is more susceptible to changes in gain. Once a desirable model has been found for the gain shifted data, the model must be shifted back by the same amount so that it overlaps with the original data. Keeping  $f_s$  ratio constant at 2, a similar error grid was constructed by varying the amount of gain shift and varying the number of desired states. Just like before, the error between the resulting model and the experimental data was evaluated at each grid point and is plotted as a colormap in Fig. 2.5. As can be seen in the figure, the best model is obtained by premultiplying the data by 40 dB. It is the case for most high order systems that a noticeably better fit to the data will occur only after a specific shift in gain. However, this shift in gain varies from system to system and cannot be predetermined.

## 2.2 Modulating the Model

The previous section outlines a method for obtaining accurate system models by manipulating the data before and after SOCIT identifies the system. This idea is taken one step further to fit data which does not start at the origin (0 Hz). Many control applications are interested only in the dynamics of a selected frequency range and so it is desirable to obtain an accurate model exclusively over these frequencies. In fact, the last three chapters of this thesis will focus exclusively on high frequency controllers. Unfortunately, SOCIT was not written for these type of applications and only identifies models which start at the origin. Similar to the undersampling problem of the last section, this problem can be overcome by manipulating the experimental data before and after use of the SOCIT routine.

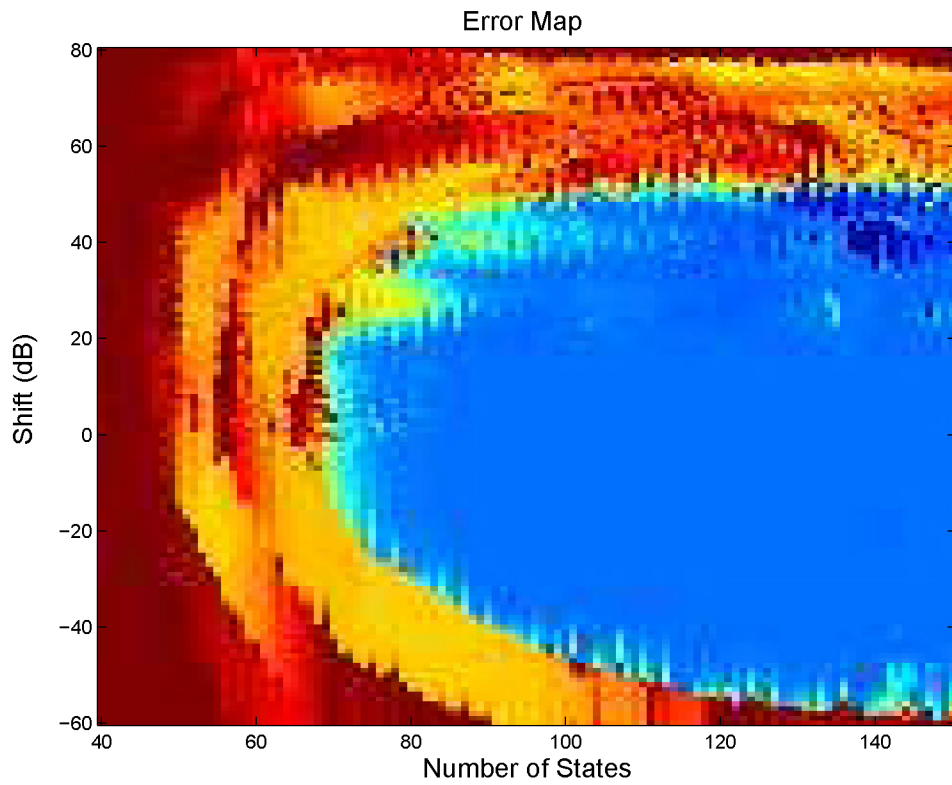


Figure 2.5 Error grid showing how changes in the gain shift of the experimental data effects the accuracy of the resulting model. Blue: Small Error, Red: Large Error.

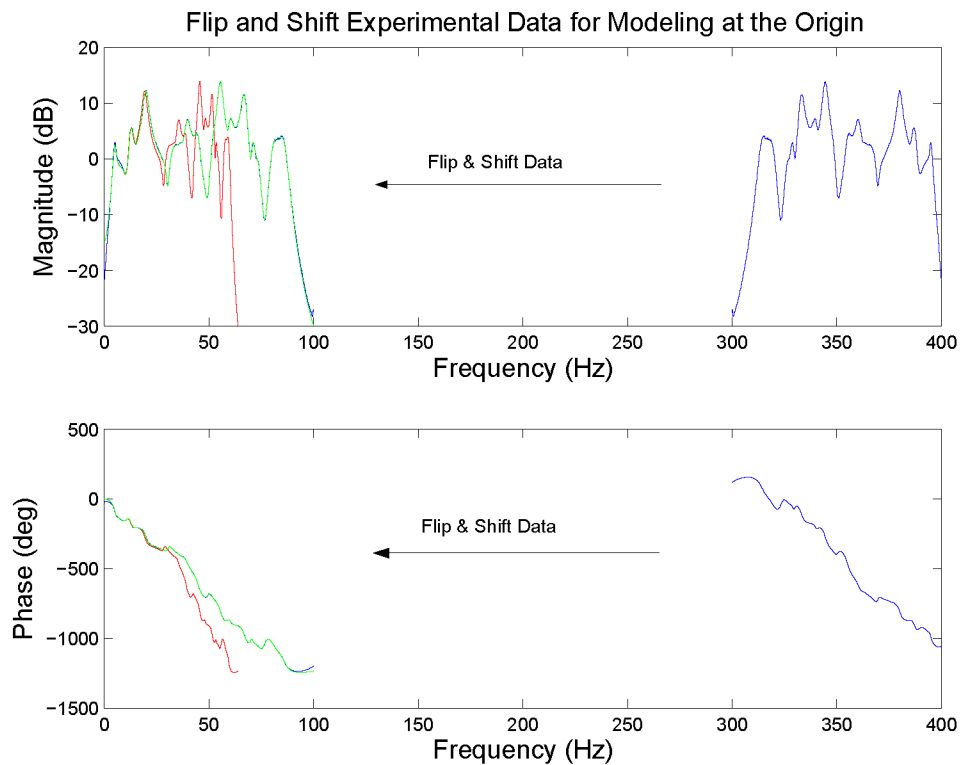


Figure 2.6 Experimental Data (blue) is flipped and shifted to the origin where it is then prewarped (red) and modelled (green) using SOCIT.

The first step in the process is to flip and shift the experimental data to the origin. This mirror image of the actual data will provide SOCIT with a usable data array for identification. Once the data is flipped and shifted, it can be prewarped and fit with a model as is shown in the previous section. This process is shown graphically in Fig. 2.6 using the data from a speaker and microphone placed in a clothing washer. The frequency range of interest for noise control of this washer was 300-400 Hz. SOCIT is now able to fit an accurate model to the data, the only problem is that the model is not in the right part of the spectrum and is also the mirror image of the actual data.

Flipping and shifting a model back to its original frequency range while retaining the integrity of the model will require a technique used primarily in communications applications called modulation. Modulation is a means for transporting a signal from

one part of the frequency spectrum to another. For example, AM radio broadcasts take audible signals from 0 Hz to 20 kHz and modulate them to a narrow frequency band somewhere from 535 kHz to 1.7 MHz. In the time domain, this is accomplished simply by multiplying the signal by a cosine oscillating at the modulation frequency. This is called modulating the signal with a carrier wave and the modulation frequency is called the carrier frequency. Eq. (2.5) shows a time-domain signal  $m(t)$  and its frequency-domain counterpart  $M(w)$ . The effect of modulation is shown in Eq. (2.6) as  $m(t)$  is multiplied by a carrier wave. The effect on  $M(w)$  is a positive and negative spectrum shift by the carrier frequency  $w_c$  (11).

$$m(t) \Leftrightarrow M(w) \quad (2.5)$$

$$m(t)(2\cos(w_c t)) \Leftrightarrow M(w + w_c) + M(w - w_c) \quad (2.6)$$

A positive and negative shift in the Laplace domain transfer function can be realized by simply replacing every  $s$  with  $s + jw_c$  and adding it to the same transfer function with  $s$  replaced by  $s - jw_c$ . A general form of transfer function modulation for a system with order  $n$  is shown in Eq. (2.7). What seems to be a straightforward mathematical manipulation of the transfer function is actually quite complicated. For many cases,  $n$  is a large number and  $w_c$  is a very large number, so calculating this formula directly will lead to numerical problems.

$$\frac{a_1(s + jw_c)^{n-1} + \dots + a_n}{(s + jw_c)^n + b_1(s + jw_c)^{n-1} + \dots + b_n} + \frac{a_1(s - jw_c)^{n-1} + \dots + a_n}{(s - jw_c)^n + b_1(s - jw_c)^{n-1} + \dots + b_n} \quad (2.7)$$

As a way to circumvent these numerical problems, it is numerically better conditioned to convert the model into its modal canonical form. Once in modal form, it is easy to break up the larger transfer function into multiple 2nd order transfer functions connected

in series. Each 2nd order transfer function can then be modulated independently of the others, free from numerical problems. A general 2nd order system is given in Eq. (2.8) and it's modulated counterpart in Eq. (2.9). Each 2nd order system expands to the 4th order system in Eq. (2.10) when modulated (all of the imaginary components of Eq. (2.9) drop out). Although this is a rather long equation, it is at least manageable when compared to modulating a large system without breaking it up into it's respective 2nd order transfer functions.

$$\frac{a_1s + a_2}{s^2 + b_1s + b_2} \Rightarrow \quad (2.8)$$

$$\frac{a_1(s + jw_c) + a_2}{(s + jw_c)^2 + b_1(s + jw_c) + b_2} + \frac{a_1(s - jw_c) + a_2}{(s - jw_c)^2 + b_1(s - jw_c) + b_2} \quad (2.9)$$

$$= \frac{2(a_1s^3 + (a_2 + a_1b_1)s^2 + (a_2b_1 + a_1(b_2 + w_c^2))s + a_2b_2 + (a_1b_1 - a_2)w_c^2)}{s^4 + 2b_1s^3 + (b_1^2 + 2(b_2 + w_c^2))s^2 + 2b_1(b_2 + w_c^2)s + (b_1^2 - 2b_2)w_c^2 + b_2^2 + w_c^4} \quad (2.10)$$

If the system has 1st order poles and zeros, they also need modulation. These states can be handled using the same method as before with the simplicity of a single pole. The general 1st order system is given in Eq. (2.11) and it's modulated counterpart in Eq. (2.12). Each 1st order system expands to the 2nd order system in Eq. (2.13) when modulated.

$$\frac{a_1s + a_2}{s + b_1} \Rightarrow \quad (2.11)$$

$$\frac{a_1(s + jw_c) + a_2}{(s + jw_c) + b_1} + \frac{a_1(s - jw_c) + a_2}{(s - jw_c) + b_1} \quad (2.12)$$

$$= \frac{2(a_1s^2 + (a_1b_1 + a_2)s + a_2b_1 + a_1w_c^2)}{s^2 + 2b_1s + b_1^2 + w_c^2} \quad (2.13)$$

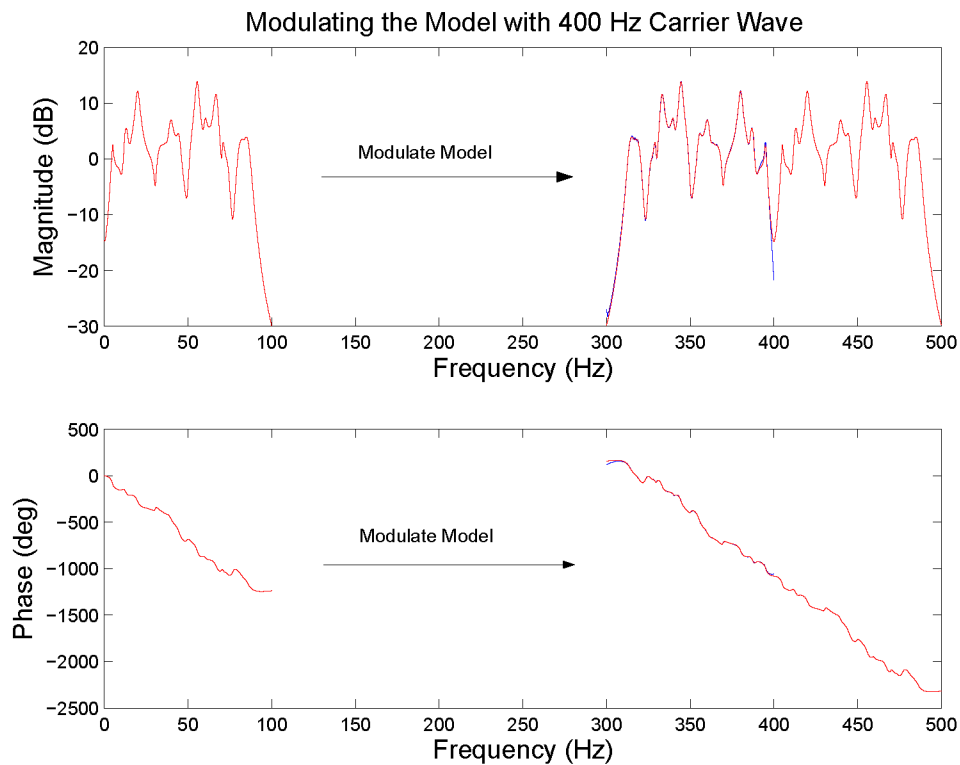


Figure 2.7 Modulating the  $n$ th order system identified at the origin results in a model of order  $2n$  centered around the carrier frequency.

Once all of the 2nd and 4th order modulated segments of the transfer function have been calculated, they can be multiplied back together again. An easy way to do this is to combine them as state-space representations connected in series. The resulting system model should now match with the original data. For the washing machine example, the SOCIT identified model at the origin was modulated with a 400 Hz carrier using the process outlined above to result in a model which matches nicely with the experimental data from 300-400 Hz (Fig. 2.7).

An obvious problem with the model of Fig. 2.7 is that it is twice the size that it needs to be to fit the experimental data. This is because during modulation, both negative and positive frequency components are shifted to the carrier frequency. A simple fix of this problem is to perform model reduction on any mode which has a frequency component

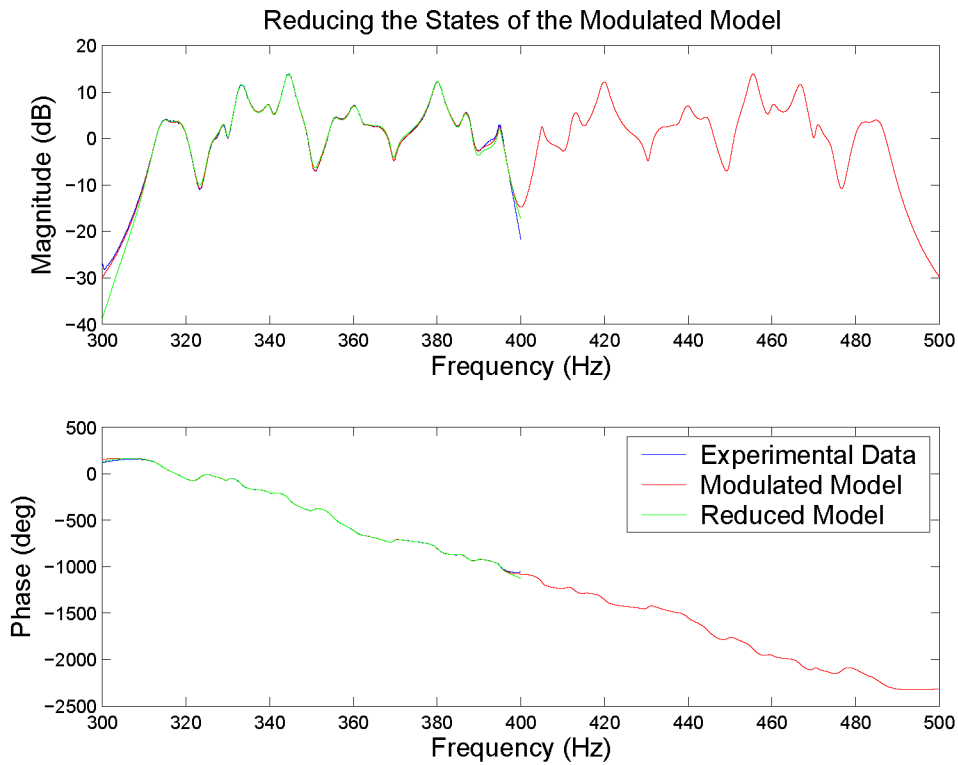


Figure 2.8 Model accuracy is maintained even after deleting all states having frequency components larger than 400 Hz.

larger than the carrier frequency. For the washing machine example, all modes above 400 Hz were deleted from the model, resulting in a reduced order model which matches the data very well (Fig. 2.8).

### 2.3 Remarks

The SOCIT algorithm for identifying system models was explored as Matlab's built-in system identification routine, *invfreqs*, was inadequate for high order modal dynamics associated with acoustics and vibrations systems. Unfortunately, SOCIT tends to yield undersampled system models which also need to be based on a frequency spectrum that contains the origin. A prewarping method of conditioning the input data was developed which solved the problem of undersampled discrete-time models and allowed for undis-

torted conversions to continuous-time models. The process of modulation expanded SOCIT's capabilities to fit models at any frequency range of interest. These two additions improved the functionality of SOCIT without tampering with SOCIT's ability to fit models to data with extremely small error.

## CHAPTER 3. Synthesis of State Weights

Optimal control theory has long been plagued by its lack of a systematic method when optimizing state and control weighting matrices used in the LQR (Linear Quadratic Regulator) cost function. Although this control is optimal for a given set of user-defined state and control weighting matrices, the performance of the controller varies widely based on the selection of these weights. Engineers have been left with the task of choosing appropriate weighting sequences by iterating each weight until the controller performs to their satisfaction. This procedure gets increasingly more frustrating and time consuming as the size of the controller increases. This chapter outlines an effective strategy to synthesize these weights and thereby reduce design time and frustration.

It is shown that the introduction of an iterative process to minimize acoustical energy in an optimization loop with LQR leads to a controller with excellent performance. A comparison is made between this automated synthesis method and the standard trial and error method. The resulting closed loop system response obtained with a controller designed using the proposed synthesis procedure shows better performance. The proposed controller design method is used to design a controller for an aircraft test panel model obtained from NASA LaRC in an effort to reduce vibrations caused by boundary layer excitation. The goal is to achieve a reduction in cabin noise by controlling the vibration of such panels. The aircraft panel model provides a good testbed for the automated state weighting procedure because of its high order dynamics.

### 3.1 Problem Description

Mitigation of aircraft cabin noise has been the topic of research for the past several decades. Several researchers have been investigating this difficult problem and various approaches have been proposed (1)(6)(20). Most of the proposed solutions have been passive approaches, but recent efforts have attempted to control both engine noise and the transmission of external noise into the cabin with actively controlled structures (3). The work described in this chapter details several control design methods for such an aircraft structure. The current experimental setup used for this investigation consists of a fuselage panel structure mounted on the wall of a transonic wind tunnel. The disturbance consists of flow-induced excitation of structural modes which the controller seeks to minimize. The ultimate goal is to reduce acoustical energy generated by structural excitation. One way to achieve that is through vibration control of the panel.

The panel structure is instrumented with four accelerometer sensors and laminated with a piezoelectric device to be used as the control actuator (Fig. 3.1). The accelerometers are placed in asymmetric positions around the piezo actuator to capture a broad range of modal responses. The controller-estimator block diagram given in Fig. 3.2 is standard for LQG regulator design. The accelerometer outputs are averaged to obtain a single output signal which is used to characterize the overall panel vibration. Although this will not produce the best controller performance, it will reduce the system from SIMO (Single-Input Multiple-Output) to SISO (Single-Input Single-Output). Since the order of the plant determines the order of the controller for LQG design, reducing the order of the plant will in turn reduce the order of the controller. Controller and closed loop system dynamics are given by the state space representations of Eq. (3.1) and Eq. (3.2), where  $L$  is the estimator gain,  $K$  is the regulator gain,  $I$  is the identity matrix, and  $B_d$  is the input matrix for the disturbance. Since there is no disturbance input available, it is reasonable to assume the plant input matrix is the same as the disturbance input

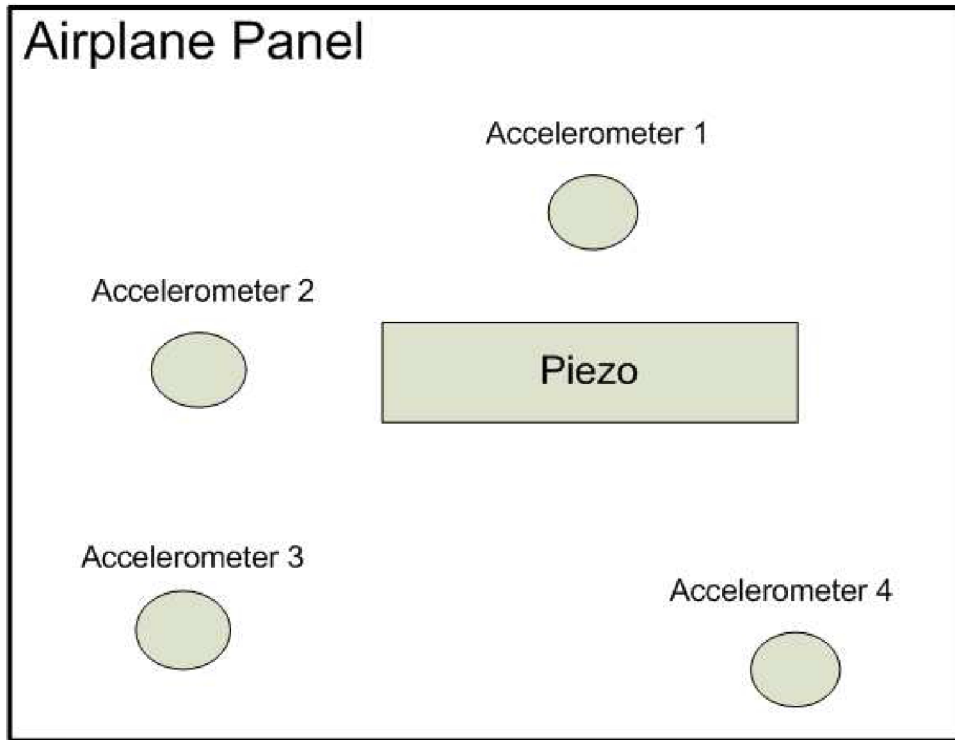


Figure 3.1 Section of airplane panel instrumented with four accelerometer sensors and one piezoelectric actuator.

matrix. Therefore, both controller design methods are evaluated using  $B_d = B$ .

$$H_{con} = \left[ \begin{array}{cc|c} A - BK - LC & & L \\ \hline & -K & 0 \end{array} \right] \quad (3.1)$$

$$H_{cl} = \left[ \begin{array}{cc|c} A & -BK & B_d \\ LC & A - BK - LC & 0 \\ \hline C & 0 & 0 \end{array} \right] \quad (3.2)$$

### 3.2 Control Design

Before proceeding to the automated synthesis of state weights in LQG (Linear Quadratic Gaussian) design, a brief background of the LQG optimization problem and solution is given. The LQG process consists of two optimization processes, the LQE

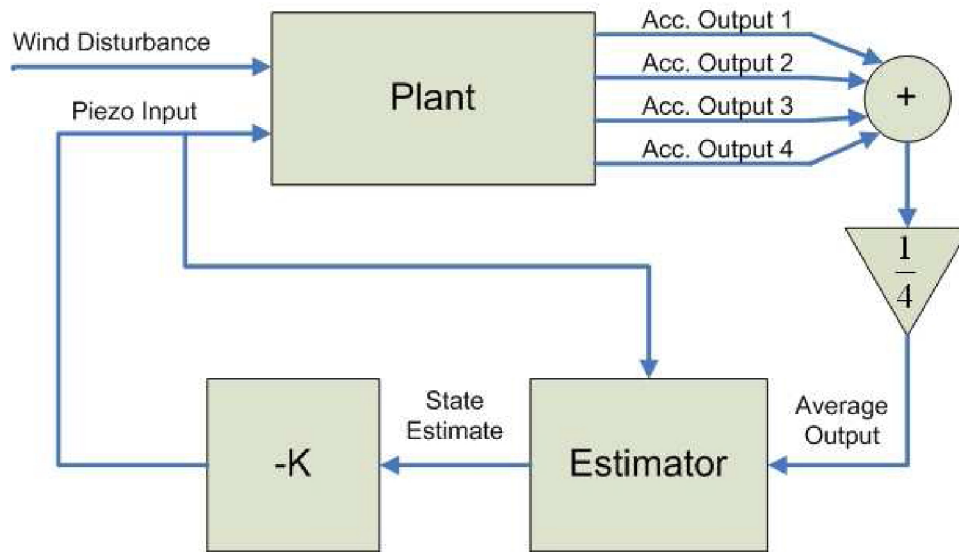


Figure 3.2 Block diagram of closed loop system.

(Linear Quadratic Estimator) and the LQR (Linear Quadratic Regulator). In relation to the aircraft panel control problem, the estimator is used to find estimates of the states using only the averaged accelerometer output and piezo input. The regulator will then apply a specified control to each of these estimated states. To understand the relation between states and the given system to be controlled, it is necessary to transform the system into its modal form. This will make each group of two states along the diagonal of the  $A$  matrix appear as a decoupled second order system with its own resonant frequency. The estimator and controller gains,  $L$  and  $K$ , can be determined individually due to the separation principle (4). Although both gains were calculated to obtain the total controller, the determination of the gain,  $K$ , will be the focus in this work.

A steady state optimal regulator works by minimizing the quadratic cost function in Eq. (3.3) subject to the state dynamics of the plant. The infinite time horizon of the integral, specific to steady state optimal control, allows the solution to take the form of constant controller gains,  $K$ . Therefore, the steady state regulator problem provides a time-invariant control law (12). In this equation,  $J$  is the performance index,  $Q$  is the state weighting matrix, and  $R$  is the control weighting matrix. Since the aircraft

panel system is a 40 state SISO model,  $Q$  will be a 40x40 matrix and  $R$  will be scalar. Although both  $R$  and  $Q$  are user defined,  $R$  can be set to any value since the only determining factor of performance is the ratio between  $Q$  and  $R$ .

$$J = \frac{1}{2} \int_0^{\infty} x(t)^T Q x(t) + u(t)^T R u(t) dt \quad (3.3)$$

$$\text{Subject to the state dynamics: } \dot{x}(t) = Ax(t) + Bu(t)$$

The quadratic cost function takes the form of the algebraic Riccati equation given in Eq. (3.4), with solution,  $S$ . If  $(A, B)$  is restricted to be controllable and  $Q$  restricted to be positive definite (all positive eigenvalues), then the existence and uniqueness of the solution,  $S$ , as well as the closed loop system's asymptotic stability are guaranteed. If these conditions are met, the Riccati equation will yield several  $S$  matrices, the one and only true solution being symmetric and positive definite. From Eq. (3.5), this solution can be used to calculate the gains of the controller,  $K$ . Similarly, the time-invariant control law of Eq. (3.6) can be used to generate control inputs based on current state estimates (12).

$$A^T S + SA - SBR^{-1}B^T S + Q = 0 \quad (3.4)$$

$$K = R^{-1}B^T S \quad (3.5)$$

$$u(t) = -K\hat{x}(t) \quad (3.6)$$

### 3.2.1 State Weighting Using Trial and Error Approach

The most common way engineers design LQR controllers is to guess values in the state weighting matrix,  $Q$ , then check the resulting closed loop performance. This is

because there is no systematic analytical methodology for finding the “best”  $Q$  matrix. Standard procedure is to transform the plant dynamics into modal state space form so that each weight has an impact on a specific resonant mode. For a regulator, increasing a weight has the effect of increasing damping at the corresponding resonant mode so that the closed loop frequency response will show a decrease in amplitude at that resonant frequency. A self-imposed limit on  $Q$  is generally made to reduce complexity. Restricting  $Q$  to be diagonal will dramatically reduce the number of weights which need to be guessed. If all entries of  $Q$  are positive, keeping diagonal form also ensures positive definiteness of  $Q$ , which ensures a solution and asymptotic stability of the closed loop system. Further reduction of the complexity of the system can be obtained by weighting both states in each mode equally. These simplifications become essential when dealing with high order controllers. The final appearance of the  $Q$  matrix is given in Eq. (3.7).

$$Q = \begin{pmatrix} q_1 & 0 & 0 & 0 & \dots & 0 & 0 \\ 0 & q_1 & 0 & 0 & \dots & 0 & 0 \\ 0 & 0 & q_2 & 0 & \dots & 0 & 0 \\ 0 & 0 & 0 & q_2 & \dots & 0 & 0 \\ \vdots & \vdots & \vdots & \vdots & \ddots & \vdots & \vdots \\ 0 & 0 & 0 & 0 & \dots & q_n & 0 \\ 0 & 0 & 0 & 0 & \dots & 0 & q_n \end{pmatrix} \quad (3.7)$$

The aircraft panel model under consideration has 40 states. Therefore, 20 sets of  $Q$  weights needed to be chosen for full state feedback. Using the trial and error method, considerable time (6 hours) was spent iterating these weights manually until a certain level of closed loop performance was achieved. The resulting simulation performance can be seen in Fig. 3.3. Energy reduction of 10.16 dB and maximum amplitude reduction of 17.67 dB were achieved.

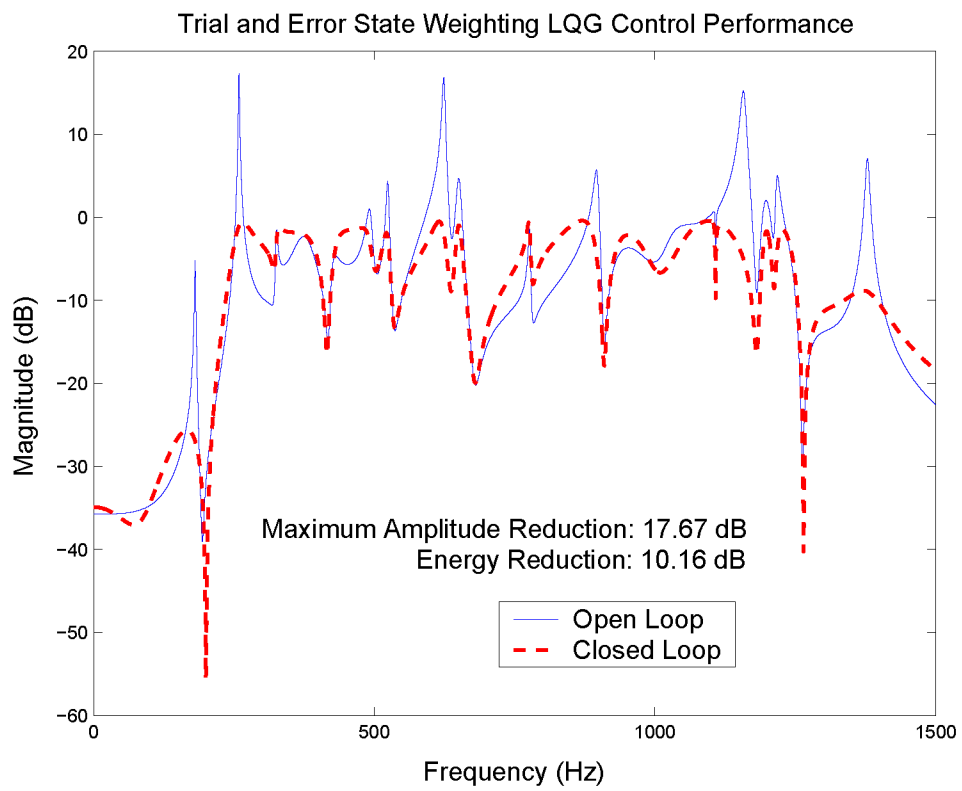


Figure 3.3 Simulation of controller reductions using state weights found by guessing and checking.

### 3.2.2 Automated State Weighting

Finding a good set of weights for  $Q$  is a tricky process, primarily because increasing one weight diminishes the effect of the others. In terms of the closed loop frequency response, damping one resonant mode will most likely cause an increase in amplitude elsewhere. This is commonly known as the “waterbed effect” for obvious reasons (18). In order to quantify broadband reductions, a new performance index must be introduced. This performance index (given in Eq. (3.8)) will be based on total energy reduction,  $E$ , and maximum peak reduction,  $M$ , across the entire frequency spectrum. The effect is that any given mode can only increase or decrease its weight if the entire spectrum benefits.

$$P = E + M \quad (3.8)$$

Automation of the state weights can begin by starting out with a reasonable initial guess of  $q = \text{diag}(C^T C)$ , where  $q$  is the diagonal vector of entries in the  $Q$  matrix and  $C$  is the plant output matrix. Once an initial  $q$  has been decided, new values of  $q$  can be found by randomly perturbing the current values of  $q$ , using these values as input into the LQR problem, and then checking to see if the closed loop system performance is better ( $P$  will increase). This can easily be implemented by the multiplicative random perturbation scheme given in Eq. (3.9), where  $N$  is random noise and gamma is a user-supplied step size.

$$q_{new} = q(1 + \gamma N) \quad (3.9)$$

Once a new  $q$  has been found, a check of the performance index is required to determine the new  $q$ 's superiority or inferiority to the old  $q$ . This can be done by looking at the sign of  $\Delta P$  in Eq. (3.10), where delta represents the change from one iteration to the next. If  $\Delta P$  is positive, the new  $q$  gives better performance, and therefore replaces

the old  $q$ . If  $\Delta P$  is negative, the new  $q$  gives worse performance, and so another random perturbation of the old  $q$  is performed.

The  $q$  weight automation problem is essentially a black-box minimization problem. For the 40 state aircraft panel problem, the global minimum exists in a 40 dimensional solution space with countless local minima. Achieving the  $q$  weights which produce this global minimum is therefore very unlikely. The  $\sigma$  in Eq. (3.10) can be used if the iteration process gets stuck in a local minima. Changing  $\sigma$  changes the performance index by increasing or decreasing the importance of energy reduction compared to maximum amplitude reduction. This will cause the current set of  $q$  weights stuck at a local minimum to move to another region of the solution space.

$$\Delta P = \sigma \Delta E + \Delta M \quad (3.10)$$

Once a desired level of performance is achieved from the random perturbations, it is possible to apply this same technique to automate the selection of controller gains. Using the sequence of controller gains corresponding to the final set of state weights as an initial guess, random perturbations according to Eq. (3.11) can be performed. The new values of  $K$  are checked against the same performance index as before (Eq. (3.8)) to determine the new  $K$ 's superiority or inferiority to the old  $K$ . Since this method directly solves for controller gains, there is no guarantee of closed loop stability as there was when iterating state weights. Therefore, an extra check of stability must be performed for each new  $K$  by making sure the controller and the closed loop system have no right-half-plane poles.

$$K_{new} = K(1 + \gamma N) \quad (3.11)$$

The implementation of this perturbation scheme can selectively iterate all modes at once, all states at once, each mode individually, or each state individually. Experiments

have shown that the performance index progressively increases in a smooth manner when the following methods of iteration are followed:

1. Iterate all modes of  $Q$  at once.
2. Iterate all states of  $Q$  at once.
3. Iterate each mode of  $Q$  individually.
4. Iterate each state of  $Q$  individually.
5. Repeat steps 1-4 with smaller step size.
6. Iterate  $K$  in the same manner as steps 1-5.

The automated state weighting procedure was used to find a controller for the aircraft panel model. Only a few minutes of time was spent on each step depending on how well the performance index progressed. An initial step size of 0.5 and a smaller step size of 0.1 were used. Within a few minutes the iteration process had determined a sequence of state weights which surpassed the performance of the trial and error method. The entire automation process took under an hour to complete. The final simulation result of the automated procedure is shown in Fig. 3.4. Energy reduction of 12.82 dB and maximum amplitude reduction of 20.16 dB were achieved.

A plot showing the energy reduction and maximum amplitude reduction progressing over the first 50 seconds of iteration is also given in Fig. 3.5. This performance was achieved by iterating all modes of  $Q$  at once with a large step size  $\gamma$  (step 1 in the iteration process). The rapid increase in both performance indices show the fast speed of the automation procedure. These plots are a good representation of any number of trials and are highly repeatable.

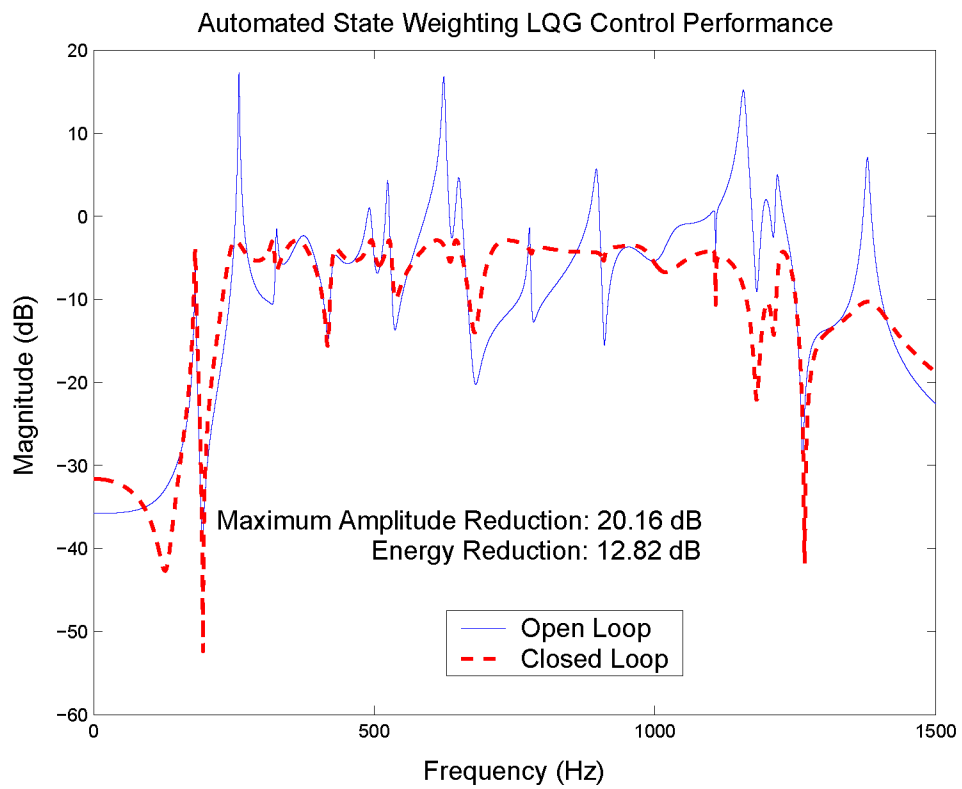


Figure 3.4 Simulation of controller reductions using state weights found by the automation method.

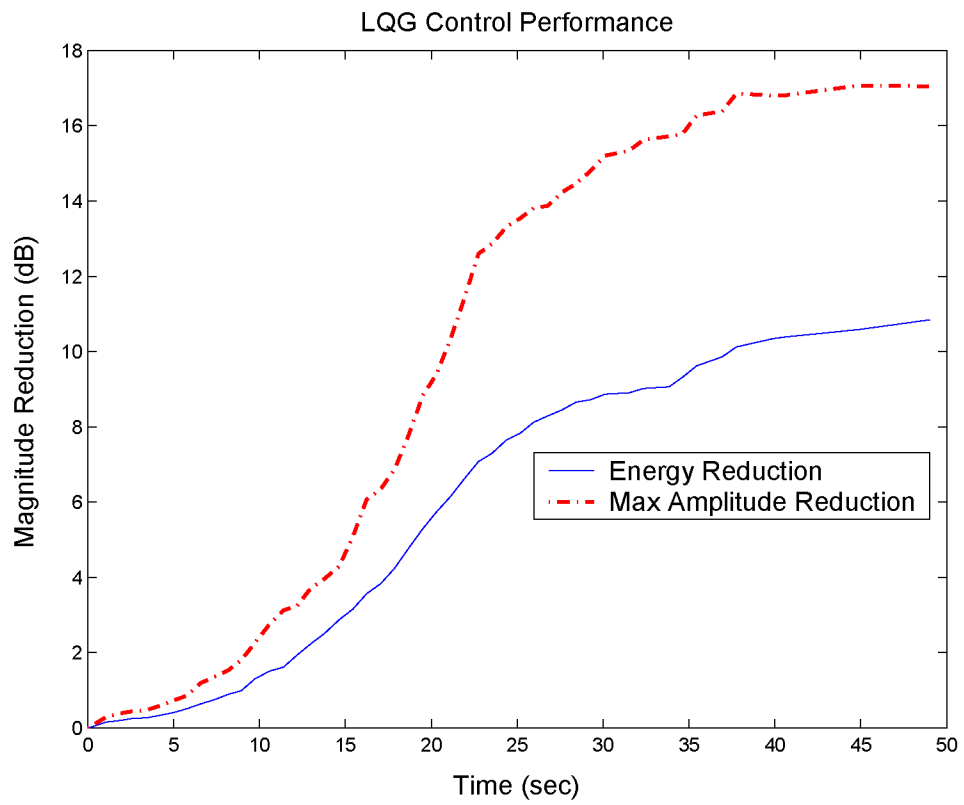


Figure 3.5 Energy and maximum amplitude reduction progressing over the first 50 seconds of iteration.

### 3.3 Remarks

A simple automated synthesis procedure outlined in this chapter significantly reduces controller design time for synthesizing the state weights used in the LQR cost function. This is especially useful for very high order controllers specific to many acoustic and vibration problems. Simulation results show an improvement of 2.66 dB in energy reduction and 2.59 dB in maximum amplitude reduction of the automated state weighting method compared to the trial and error method. In addition to having better performance, the automated synthesis method consistently determined the controller gains in much shorter time than that taken by the trial and error method. The final results are shown in Table 3.1.

Method	Energy Reduction	Max. Amp. Reduction	Time Spent
Trial and Error	10.16 dB	17.67 dB	6 hrs.
Automation	12.82 dB	20.16 dB	30 mins.

Table 3.1 Comparison of the two methods.

## CHAPTER 4. In-Seat Active Noise Control

This chapter deals with the active control of noise using the experimental setup shown in Fig. 4.1 where a mannequin is used to simulate a human and the active control system is placed in the headrest of a seat. The configuration is used to simulate an environment in which a person is sitting in a chair or seat in noisy surroundings. Although several active noise control schemes have been employed in a headrest (16)(17), none have been successful in the high frequency range. In fact, nearly all active noise control devices are limited in their control to below 1000 Hz. This is partly due to the fact that passive noise control approaches work well at these high frequencies, so active systems are primarily implemented in the low frequencies where passive techniques aren't as capable. At high frequencies, large noise reductions occur with the simple use of lightweight foam. At low frequencies, however, sound obey's the mass law and will only show significant reductions by impeding it's path with a significant amount of mass (2). In many applications this is very impractical, so replacing the large mass with a speaker, microphone, and controller becomes appealing. Many noise control solutions will typically employ both active and passive systems to achieve broadband noise reduction.

The goal of this chapter is to achieve active noise control in the high frequency region ( $>1000$  Hz). This is important for applications in which passive techniques are impossible or impractical to implement. In the case of passive headsets, often times the user is uncomfortable wearing them and as a result he/she foregoes any hearing protection at all. An active headrest system would allow these users to be free of an uncomfortable headset and still prevent hearing loss at the same time. Active systems

can also be used as additional noise reduction if the disturbance is very loud in the high frequency region. A benefit of using a combined active and passive system is that their effects are essentially additive. For example, if a disturbance can be reduced by 20 dB through passive means and 20 dB through active means, both systems working together can achieve 40 dB of noise reduction.

The experimental setup of Fig. 4.1 involves two speakers built into the headrest. The speaker on the left is used as a source of disturbance noise and the speaker on the right is used as the control speaker. Although two microphones are seen in the figure, only one is used as the controller feedback microphone. The mannequin from HEAD Acoustics mimics the acoustic impedance of a real human head and shoulders. It comes equipped with microphones in the ears and audio amplification and processing which matches more closely to the human perception of sound (7). These microphones will be used to evaluate the controller's performance, measuring noise reduction in a way which closely resembles what an actual person might perceive.

## 4.1 Broadband Control

An attempt at achieving broadband control was initiated by first experimentally determining the frequency response function from control speaker to performance microphone. Although using the performance microphone as the control microphone is not realistic, it's the first step toward proving a concept. Once a controller is shown to work with the control microphone in the ear, the microphone can be moved further away.

The speaker to microphone transfer function (Fig. 4.2) shows no modal behavior (i.e. no resonant peaks) as compared with most acoustical or vibrational systems. This can be attributed to both the high frequency range in which the transfer function was obtained and the fact that this response was taken in a free field. It is because of the latter that most active noise control systems are implemented in an enclosed structure.

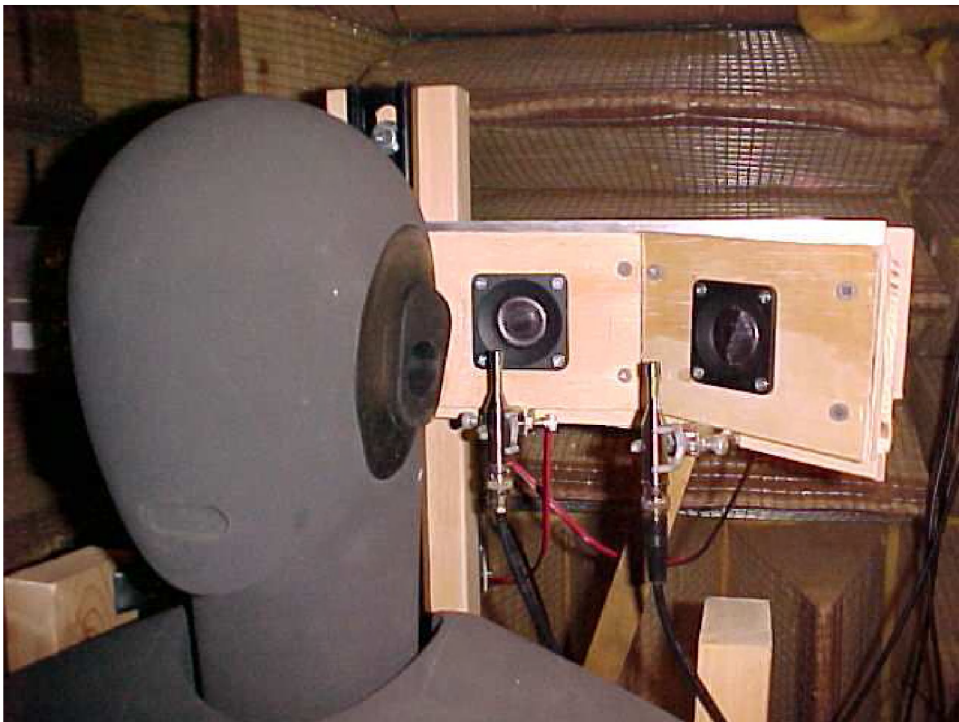


Figure 4.1 The active headrest experimental setup using a dummy head in an anechoic chamber.

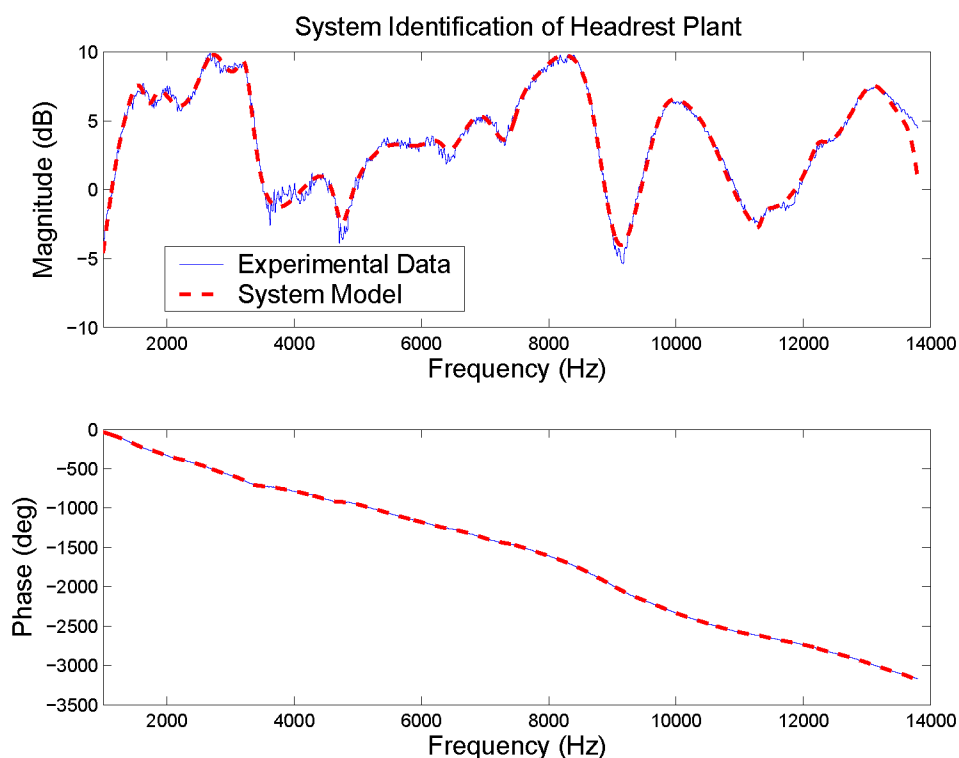


Figure 4.2 40th order model shows a very flat magnitude response and a large phase delay over the entire frequency range.

Enclosures provide both resonant modes and quiet nodes at frequencies determined by the dimensions of the enclosure (13). It is the resonant modes of the enclosure which are targeted for damping by the controller. Since there are no resonant modes to damp in the free field, it becomes very difficult to actively control the sound. Although feedforward control in the free field is achievable (9), its basic premise of signal inversion is limited to low frequencies.

Another important thing to note about the speaker to microphone transfer function is the extreme phase delay exhibited in the response. This sizeable delay is largely attributed to the physical distance between the speaker and the microphone and therefore cannot be reduced without tampering with the headrest setup. The pole-zero map of the system (Fig. 4.3) shows many nonminimum phase zeros (i.e. zeros in the right half plane). Nonminimum phase zeros are detrimental to feedback control because increas-

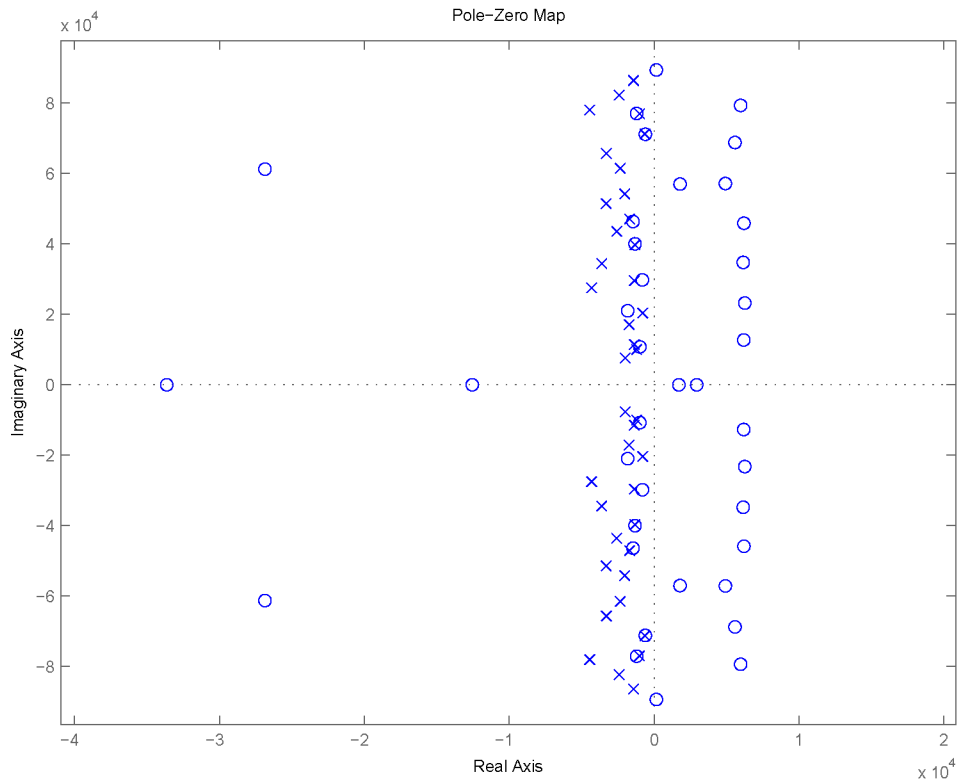


Figure 4.3 Pole-zero mapping of the transfer function of the system reveals many right-half-plane zeros.

ing the gain of the controller moves the poles closer to the right half plane zeros. This actually decreases the damping of the system, making the disturbance louder. If the gain is increased too much, it will make the closed loop system unstable.

A simulation of the broadband LQG closed loop performance using the headrest model is shown in Fig. 4.4. The controller achieves just 1-2 dB of reduction at the key peaks. The difficulty comes from a lack of large resonant modes to damp and a large phase delay which severely limits the control authority. The next section will introduce a different type of controller which performs well even under these physical limitations.

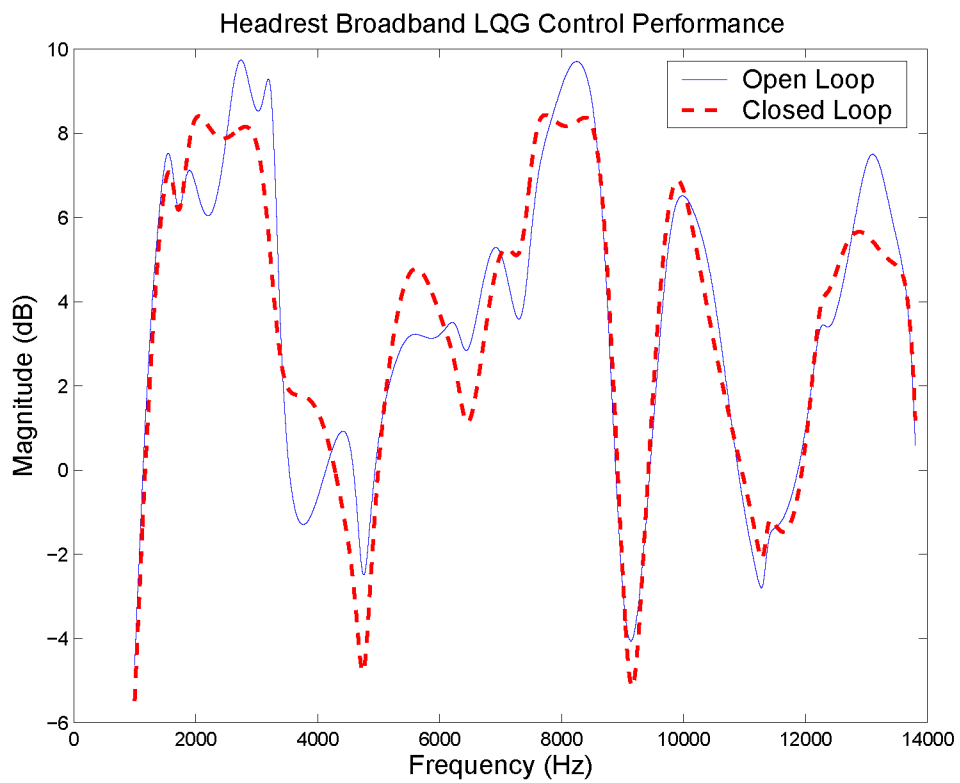


Figure 4.4 Only 1-2 dB of reduction achievable because of nearly flat free field dynamics and a large phase delay.

## 4.2 Resonant Mode Control

Due to a lack of resonant modes in the open loop response of the system, the focus shifted from trying to exert control across the entire frequency band to focusing control effort in a narrow frequency region. One control technique known for having very effective control in a narrow frequency band is called a resonant mode controller. Resonant mode control is generally a frequency tunable second order filter used to provide maximum damping to a resonant peak of a system (15). Large damping over a narrow frequency band has great appeal for tonal noise control applications because of its ability to reduce a tonal noise without increasing the noise at other parts of the spectrum. For a free field acoustics problem such as the speaker/microphone system above, the question arises: how can a resonant mode controller provide damping to a system's resonant modes if no resonant modes are present in the system?

One solution to the question posed above is the introduction of an artificial resonant mode into the system. This resonant mode is not part of the acoustical transfer function, but instead is inserted as a digital filter in series with the actual system. When the frequency response of the entire system is obtained, it now has essentially one large resonant mode corresponding to the digital filter's resonant peak. This modal frequency response data can now be fit with a second order transfer function. Since this transfer function has a resonant peak, a controller can be designed using the LQG algorithm to increase the damping of the artificial mode created by the second order filter. Therefore, the resulting controller becomes the LQG controller multiplied by the second order filter. This might seem like a strange way to go about synthesizing a resonant mode controller, but the LQG algorithm is only effective for modal systems and there are no discernable modes in a free field acoustics problem. A more in-depth explanation of this process is given in the next section.

### 4.2.1 Controller Design

The second order resonant mode filter used to augment the plant was designed according to Eq. (4.1). The zero was chosen to be the same distance along the real axis as the resonant pole was from the origin to make the filter symmetric. The value of  $\sigma$  is defined as  $\sigma = \zeta w_d / \sqrt{1 - \zeta^2}$ , where  $\zeta$  is the damping and  $w_d$  is the damped natural frequency of the filter ( $\sigma$  is also defined as the shortest distance between the  $iw$ -axis and the complex pole) (5).  $\sigma$  was chosen instead of  $\zeta$  to be the main user-specified variable because a constant  $\sigma$  yields identically shaped resonant mode filters for any  $w_d$ , whereas a constant  $\zeta$  stretches it's shape as  $w_d$  is varied. The constant out front was derived to keep the magnitude of the peak of the filter at 0 dB. Using this equation provides a quick way of obtaining a second order filter which has a shape dependent only on the user-specified value of  $\sigma$ . It's magnitude remains at 0 dB and it's shape consistent for all frequencies.

$$F_{res} = \left( \frac{2\sigma}{\sqrt{2}} \right) \frac{s + w_d}{s^2 + 2\sigma s + w_d^2} \quad (4.1)$$

Once a filter is designed at a particular frequency, it can be converted to a discrete model and placed in series with the speaker/microphone system so that a frequency response can be taken with the filter in the loop. System identification can then be performed on the frequency response to obtain a second order model of the augmented plant,  $G_a$  (Eq. (4.2)).

$$G_a = F_{res}G \quad (4.2)$$

A controller can then be obtained with the LQG optimization algorithm using the augmented plant matrices (Eq. (4.3)). This controller is generally an extremely damped second order system which essentially serves the purpose of shifting the gain and phase of the augmented plant. This indicates that the resulting controller, found by multiplying

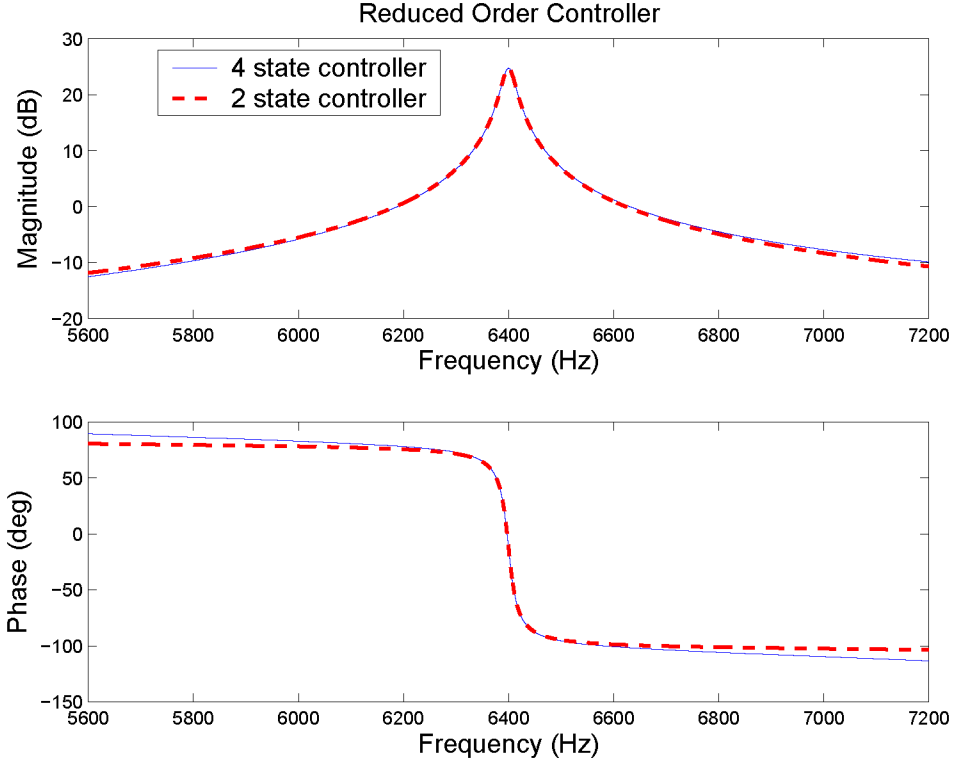


Figure 4.5 4th order controller and 2nd order reduced controller show almost no difference.

the resonant filter with the LQG controller (Eq. (4.4)), is essentially a gain and phase shifted version of the augmented plant. It is due to this fact that the fourth order controller  $H_{con}$  can always be reduced to second order without hindering its effect. A sample controller designed for 6400 Hz is shown in Fig. 4.5 with its fourth order counterpart.

$$H_{LQGcon} = \left[ \begin{array}{c|c} A_a - B_a K - LC_a & L \\ \hline -K & 0 \end{array} \right] \quad (4.3)$$

$$H_{con} = F_{res} H_{LQGcon} \quad (4.4)$$

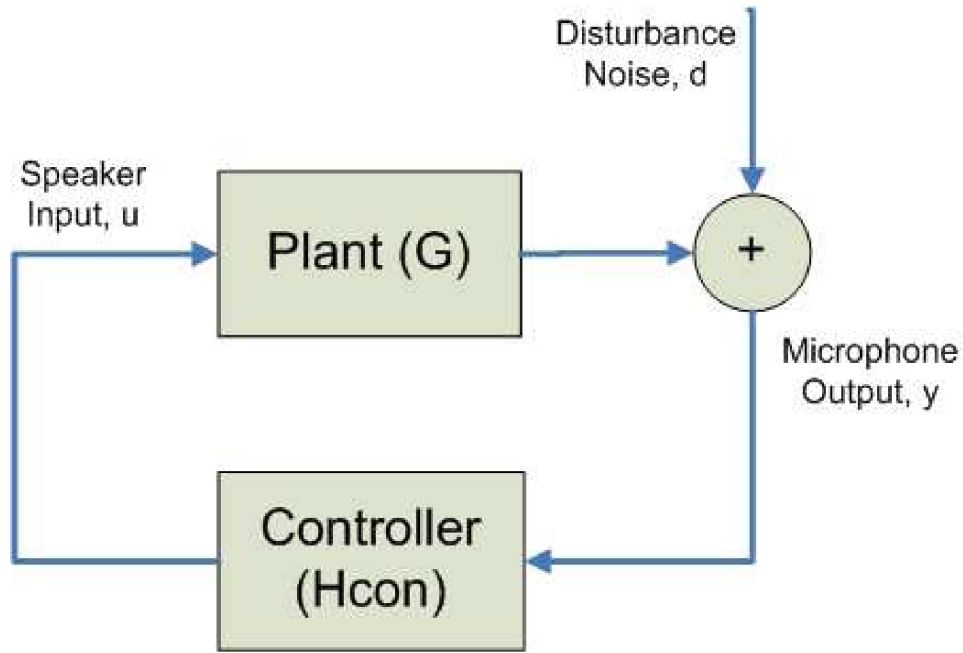


Figure 4.6 Resonant Mode Controller Block Diagram.

#### 4.2.2 Controller Performance

A block diagram of the closed loop system is shown in Fig. 4.6. This is the final configuration where the “Controller” block consists of the reduced resonant mode controller,  $H_{con}$ , while the “Plant” block is simply the speaker to microphone transfer function. The closed loop performance was derived by inspection of this block diagram and is given in Eq. (4.5). Keep in mind the control and estimator gains,  $K$  and  $L$ , are the same as in Eq. (4.3) and not the gains of the final reduced controller,  $H_{con}$ . The closed loop performance of the resonant mode controller was simulated in Fig. 4.7. Notice that this is basically the inverse of the resonant mode controller magnitude plot. The effect of the controller on the disturbance noise is essentially a notch filter. Therefore, if the noise is primarily tonal, the controller will have a substantial effect on reducing the overall noise level.

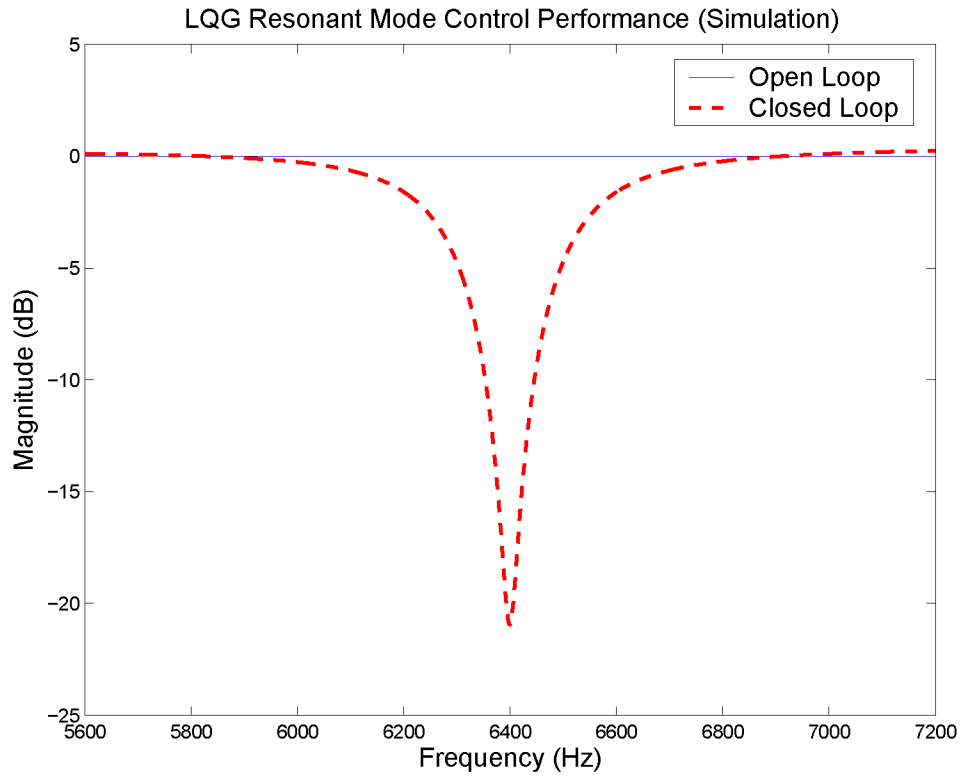


Figure 4.7 Simulation of white noise disturbance with controller on and off.

$$H_{cl} = \left[ \begin{array}{cc|c} A_a & -B_a K & 0 \\ LC_a & A_a - B_a K - LC_a & L \\ \hline C_a & 0 & 1 \end{array} \right] \quad (4.5)$$

The resonant mode control scheme outlined above was implemented in real-time on the headrest setup using the dSpace data acquisition system. The disturbance noise was white noise generated by the speaker on the left in Fig. 4.1 and the speaker used for control is the one on the right. Notice that the disturbance speaker is physically closer to the ear than the control speaker. While this presents a problem for feedforward control, it makes little difference in feedback control. The control performance was evaluated with the error/control microphone positioned at varying distances from the performance microphone (ear) in Fig. 4.8. As can be seen in the figure, desired reductions were

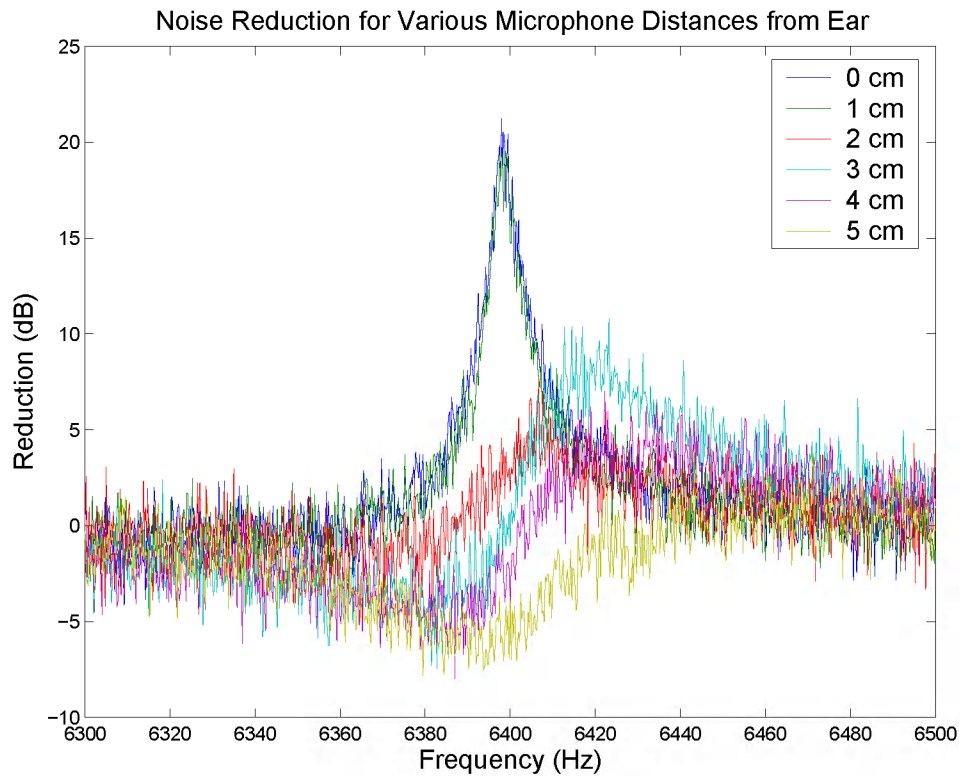


Figure 4.8 Error microphone must be positioned within 1 cm of the ear to achieve desired performance.

achieved when the error microphone was positioned within 1 cm of the performance microphone. However, at further distances the performance degraded substantially. At 5 cm the control effort actually increased the level of noise.

As a demonstration of why the “region of quiet” around the error microphone is so small, a simulation showing the perfect cancellation of a 6400 Hz tone is given in Fig. 4.9. Assuming the disturbance noise and the control signal are perpendicularly intersecting plane waves, the biggest possible region where reduction occurs is shown to have a 1 cm radius. The size of this quiet region is of course directly proportional to the wavelength of the frequency being cancelled. As an example, the radius of the quiet region at 640 Hz is 10 cm as compared to the 1 cm quiet region exhibited at 6400 Hz. Therefore, when controlling low frequencies, the error microphone can be placed much

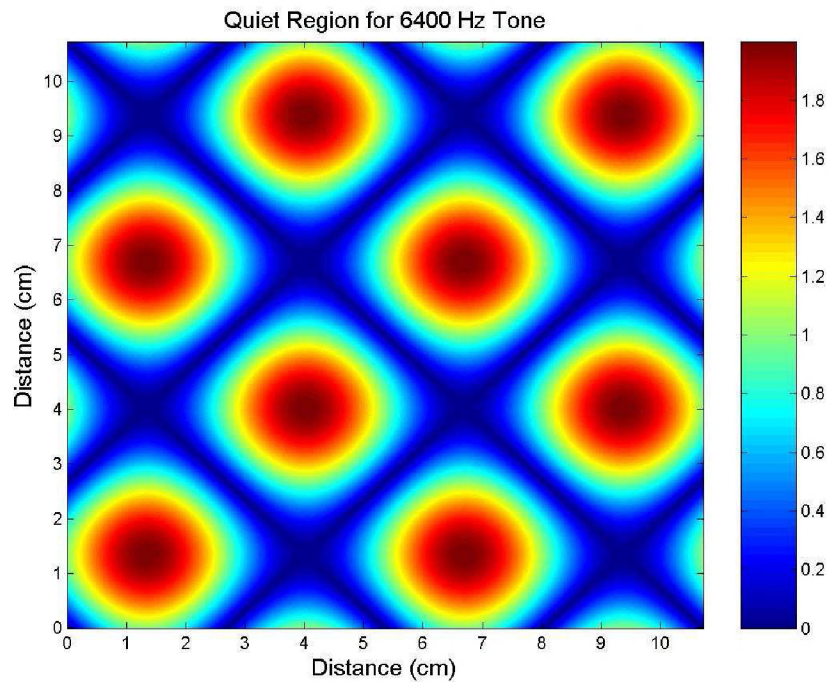


Figure 4.9 Simulation showing the 1 cm radius quiet regions possible with perfect cancellation at 6400 Hz. Quiet regions are in blue. Noise is increased in red regions.

further away from the listener than when controlling high frequencies.

Due to the lack of spatial invariance inherent in high frequency controllers, a different setup is needed. With a quiet region so small, even the slightest movement from the listener's head would cause extreme changes in performance. Even if the microphone was attached to the listener's ear, movement of the head would dramatically change the transfer function between speaker and microphone. This high uncertainty in the plant model would lead to a less robust control system which could potentially be driven to instability.

### 4.3 Remarks

An in-seat active noise control setup was investigated as a means of controlling high frequency disturbances. Due to the free field nature of the acoustics problem, the system did not have any noticeable resonant mode characteristics, and accordingly, little control action could be exerted. An alternative method of resonant mode control was proposed to exert some control authority over a narrow frequency band. This alternative method of control succeeded in creating a notch in the disturbance spectrum at any desired frequency. This type of controller was found to be ideal for reducing high frequency tonal noise. Unfortunately, the region of silence surrounding the error microphone was found to be very small at high frequencies, requiring the microphone distance from the listener's ear be very small.

## CHAPTER 5. Adaptive Resonant Mode Control

Although the headrest setup of the previous chapter was technically successful at reducing high frequency tonal noise, the physical restrictions imposed by the setup caused many serious impracticalities. As this chapter will show, these limitations can be overcome through the use of a headset active noise control system. A headset system has four important advantages over a headrest system:

1. The speaker is much closer to the error microphone. Decreasing this distance substantially lowers the phase lag of the resulting control frequency response. Less phase lag in the frequency response leads to a system model with fewer nonminimum phase zeros. Fewer nonminimum phase zeros enables more control action to be taken and therefore results in better controller performance.
2. The microphone is much closer to the ear. The microphone can be easily positioned very close listener's ear, perhaps even placed at the opening of the ear canal similar to an earbud speaker. This is very important considering the small quiet region of control exhibited at high frequencies ( $< 2$  cm at 6400 Hz).
3. The distance between the speaker and microphone is fixed. Having a fixed distance from speaker to microphone ensures less variability in the control transfer function. In the headrest system, any movement of the listener's head would lead to dramatic changes in the control transfer function, making the controller performance highly dependent on keeping the listener confined to one location. A headset system

would allow unlimited head movement because the control system would move along with the listener's head.

4. The speaker to microphone path is less likely to be obstructed. In the headrest setup, an object such as the listener's hand could easily get between the speaker and microphone. Incorporating uncertainties such as these into the headrest plant model would be required to ensure closed loop stability. Unfortunately, this increased robustness comes at the cost of decreased performance. A headset system's plant model uncertainty would be much lower and would therefore have better performance.

## 5.1 Experimental Setup

Due to the small size of components necessary for a headset active noise control device, the same speakers and microphones used in the headrest experiment could not be used for the headset. Instead, inexpensive miniature speakers and microphones were used to keep the design as compact as possible. The speaker used in the headset was chosen to be a notebook computer speaker because of its high output power and clarity. Electret condenser microphones were chosen because of their small size and high signal-to-noise ratio. The new speaker required no amplification due to its small size (unlike the headrest speakers), but a separate amplifier circuit needed to be built to amplify the microphone signals.

The electret microphone amplifier circuit schematic is shown in Fig. 5.1. The amplifier required a 6-15 Volt supply and the microphones required 2 Volts. These were both accommodated with one 9 Volt battery by using a voltage divider before connection with the microphones. The microphone's output is then an AC signal offset with a DC voltage (2 Volts). The microphone output is connected to a high pass filter to get rid of the DC offset both before and after amplification to ensure only the AC signal remains

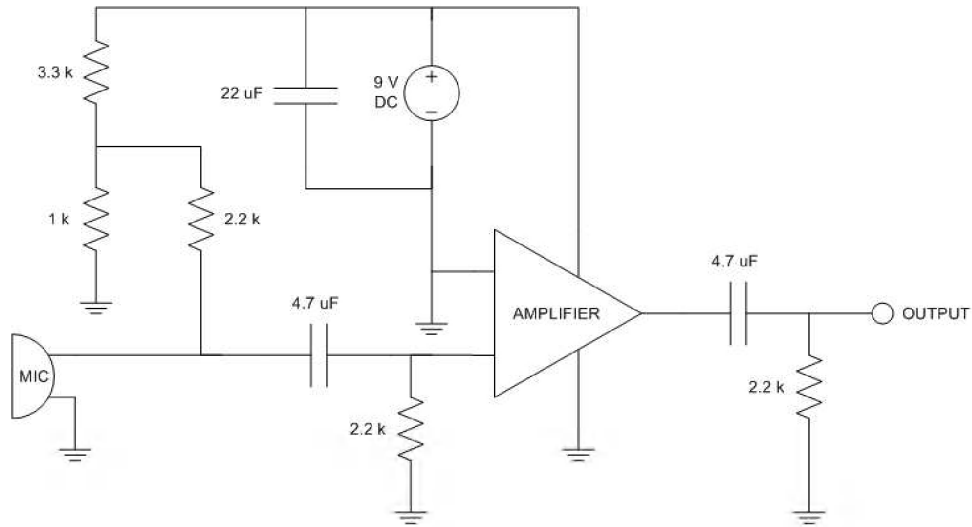


Figure 5.1 Electret microphone amplifier circuit schematic.

in the final output. Two of these circuits were put into a circuit box for amplification of both the feedback and feedforward microphones (Fig. 5.2).

The experiment design uses the same mannequin as in the headrest experiment. The headset speaker is attached to a wooden beam which extends from the side of the headrest to just a few centimeters from the outer ear of the dummy. Fig. 5.3 shows the speaker facing toward the ear with the feedforward microphone glued to the back of it and facing the opposite direction. The feedback microphone is taped to the inside of the dummy ear canal and is facing the performance microphone in the ear. This setup is almost entirely active since there are no passive materials blocking the path from a disturbance noise to the performance microphone except for the speaker and the feedback microphone themselves.

## 5.2 Control Design

A new closed form solution for a resonant mode controller is derived in this section which vastly simplifies the controller design process. This solution allows for the user to decide the robustness of the control by setting the gain margin for the loop transfer



Figure 5.2 Microphones and microphone filter/amplifier box.

function ahead of time. The only design parameter is  $\sigma$ , which essentially determines the shape of the resonant mode controller and consequently the shape of the resulting notch in the noise spectrum.

The plant and controller configuration is unchanged from Fig. 4.6 of the previous chapter. Inspection of this block diagram will show the disturbance transfer function to be that of Eq. (5.1). It is clear from looking at this equation that the loop transfer function,  $GH_{con}$ , needs to be a large and negative value at the resonant frequency in order to minimize the effect of the disturbance at that frequency. Therefore, for optimum disturbance rejection at the resonant frequency,  $w_r$ , the magnitude should be large and the phase should be at  $\pm\pi$  radians.

$$\frac{y}{d} = \frac{1}{1 - GH_{con}} \quad (5.1)$$

By assuming the plant,  $G$ , to be of constant gain and phase around a small neighbor-

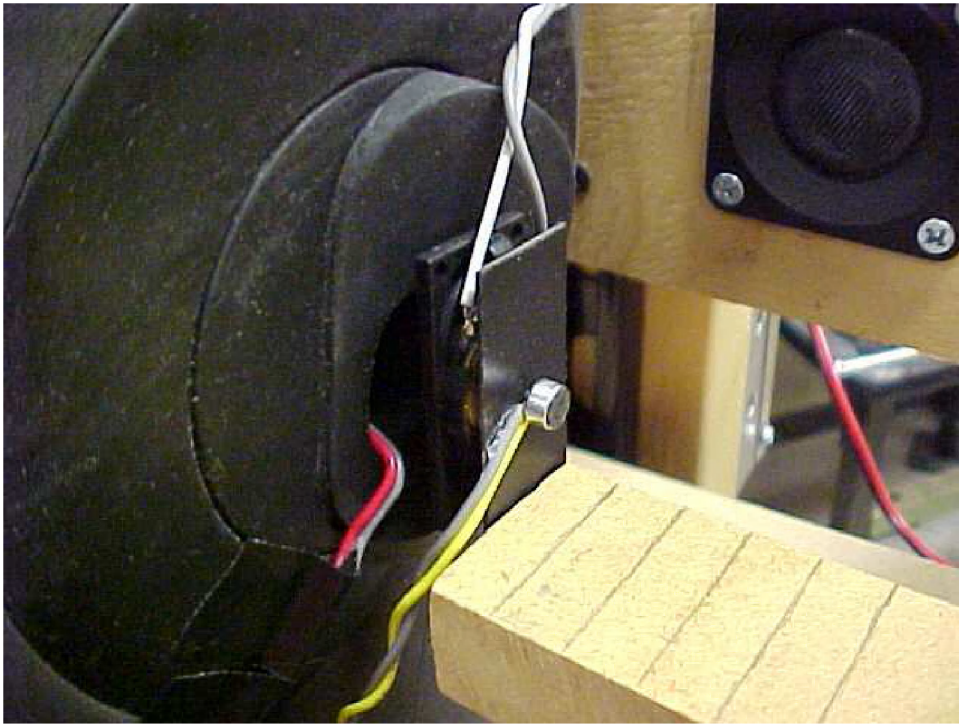


Figure 5.3 Headset setup with feedback microphone (red wire) in the dummy ear and feedforward microphone (yellow wire) and speaker (white wire) just outside the ear.

hood of the resonant mode, the structure of the controller,  $H_{con}$ , and the loop transfer function,  $GH_{con}$ , can each take the form of a second order resonant mode. This is a reasonable assumption if the resonant mode is chosen to be very undamped (small  $\sigma$ ) so the controller gain is very small everywhere except for the resonant peak. Also, the headset system magnitude response is very flat due to the free field nature of the setup and the phase delay is fairly small because of the close proximity between the speaker and feedback microphone. Since each second order resonant mode transfer function is identical in structure, the only difference between controllers is their magnitude and phase at the peak ( $w_r$ ). Therefore, to completely describe the controller,  $H_{con}$ , one only needs to know it's magnitude and phase at the resonant peak. To determine the magnitude and phase of the controller which will lead to the desired loop response, it becomes necessary to solve Eq. (5.2) in terms of both it's magnitude and it's phase evaluated at  $w_r$  (Eq. (5.3)(5.4)).

$$H_{con} = \frac{GH_{con}}{G} \quad (5.2)$$

$$g = |H_{con}(w_r)| = \frac{|GH_{con}(w_r)|}{|G(w_r)|} = \frac{1/\mathbf{GM}}{|G(w_r)|} \quad (5.3)$$

$$\phi = \angle H_{con}(w_r) = \angle GH_{con}(w_r) - \angle G(w_r) = \pi - \angle G(w_r) \quad (5.4)$$

Eq. (5.3) shows the magnitude of the loop at  $w_r$  is just the reciprocal of the gain margin,  $\mathbf{GM}$ , and therefore, the controller gain can be directly determined by a user specified gain margin. The desired phase of the loop is shown in Eq. (5.4) to be  $\pi$  radians to ensure negative feedback and maximum disturbance rejection. Note that a plant model is not required in this type of control since the only values needed are the experimentally obtained frequency response magnitude and phase. Using these two

equations enables the direct computation of the magnitude and phase of the controller given only the frequency response data of the plant.

Once the magnitude and phase of the controller at the resonant frequency are calculated, the next step is finding a second order transfer function which will exhibit this same magnitude and phase at it's resonant frequency. Eq. (5.5) shows the general second order transfer function of the controller in the discrete domain with sampling time,  $T$ . The desired magnitude and phase of the controller at resonance will each respectively determine the unknown value of gain,  $k$ , and the unknown zero location,  $a$ . The following work will derive a closed form solution for  $k$  and  $a$ , given the desired gain,  $g$ , and phase,  $\phi$ , of the controller. Once values for  $k$  and  $a$  have been calculated,  $H_{con}$  is known completely.

$$H_{con} = \frac{k(z - a)}{z^2 - 2ze^{-\sigma T}\cos(w_r T) + e^{-2\sigma T}} \quad (5.5)$$

When solving for the magnitude and phase of the transfer function in Eq. (5.5) it becomes necessary to split it into it's real and imaginary parts, as in Eq. (5.6). Once this is done, the phase calculation can be made for a general phase,  $\phi$ , as is shown in Eq. (5.7) and (5.8). Note that the gain,  $k$ , drops out of this equation. This allows for the direct calculation of the zero location,  $a$ , in terms of the desired phase,  $\phi$ .

$$H_{con}(w_r) = \frac{k(\cos(w_r T) - a + j\sin(w_r T))}{(1 - e^{-\sigma T})\cos(2w_r T) - e^{-\sigma T} + e^{-2\sigma T} + j(1 - e^{-\sigma T})\sin(2w_r T)} \quad (5.6)$$

$$\phi = \angle H_{con}(w_r) \quad (5.7)$$

$$\phi = \tan^{-1}\left(\frac{\sin(w_r T)}{\cos(w_r T) - a}\right) - \tan^{-1}\left(\frac{(1 - e^{-\sigma T})\sin(2w_r T)}{(1 - e^{-\sigma T})\cos(2w_r T) - e^{-\sigma T} + e^{-2\sigma T}}\right) \quad (5.8)$$

$$a = \frac{e^{-\sigma T} \sin(\phi - w_r T) - \sin(\phi + w_r T)}{e^{-\sigma T} \sin(\phi) - \sin(\phi + 2w_r T)} \quad (5.9)$$

Looking back at Eq. (5.6), a general gain,  $g$ , can be calculated as shown in Eq. (5.10) and (5.11). This is then solved for the controller gain,  $k$ , in terms of the zero location,  $a$ , and the magnitude at resonance,  $g$ , in Eq. (5.12).

$$g = |H_{con}(w_r)| \quad (5.10)$$

$$g = \frac{k \sqrt{(\cos(w_r T) - a)^2 + \sin^2(w_r T)}}{\sqrt{((1 - e^{-\sigma T}) \cos(2w_r T) + e^{-2\sigma T} - e^{-\sigma T})^2 + ((1 - e^{-\sigma T}) \sin(2w_r T))^2}} \quad (5.11)$$

$$k = \frac{g \sqrt{((1 - e^{-\sigma T}) \cos(2w_r T) + e^{-2\sigma T} - e^{-\sigma T})^2 + ((1 - e^{-\sigma T}) \sin(2w_r T))^2}}{\sqrt{a^2 - 2a \cos(w_r T) + 1}} \quad (5.12)$$

Now that the unknowns,  $a$  and  $k$ , are explicitly solved for in Eq. (5.9) and (5.12), the controller defined in Eq. (5.5) has a closed form solution. Finally, substituting for  $g$  and  $\phi$ ,  $H_{con}$  can be written in terms of the magnitude and phase of the plant at the resonant frequency (Eq. (5.13)-(5.15)). This means the entire transfer function of  $H_{con}$  can be calculated using only the plant frequency response data as input. The designer is able to specify the sampling time,  $T$ , the controller shape (given by  $\sigma$ ), and most importantly the gain margin of the resulting loop transfer function, **GM**. Fig. 5.4 shows an example loop response at 6400 Hz by setting the gain margin to 6 dB.

$$H_{con} = \frac{k(z - a)}{z^2 - 2ze^{-\sigma T} \cos(w_r T) + e^{-2\sigma T}} \quad \text{where:} \quad (5.13)$$

$$a = \frac{e^{-\sigma T} \sin(w_r T + \angle G(w_r)) + \sin(w_r T - \angle G(w_r))}{e^{-\sigma T} \sin(\angle G(w_r)) + \sin(2w_r T - \angle G(w_r))} \quad (5.14)$$

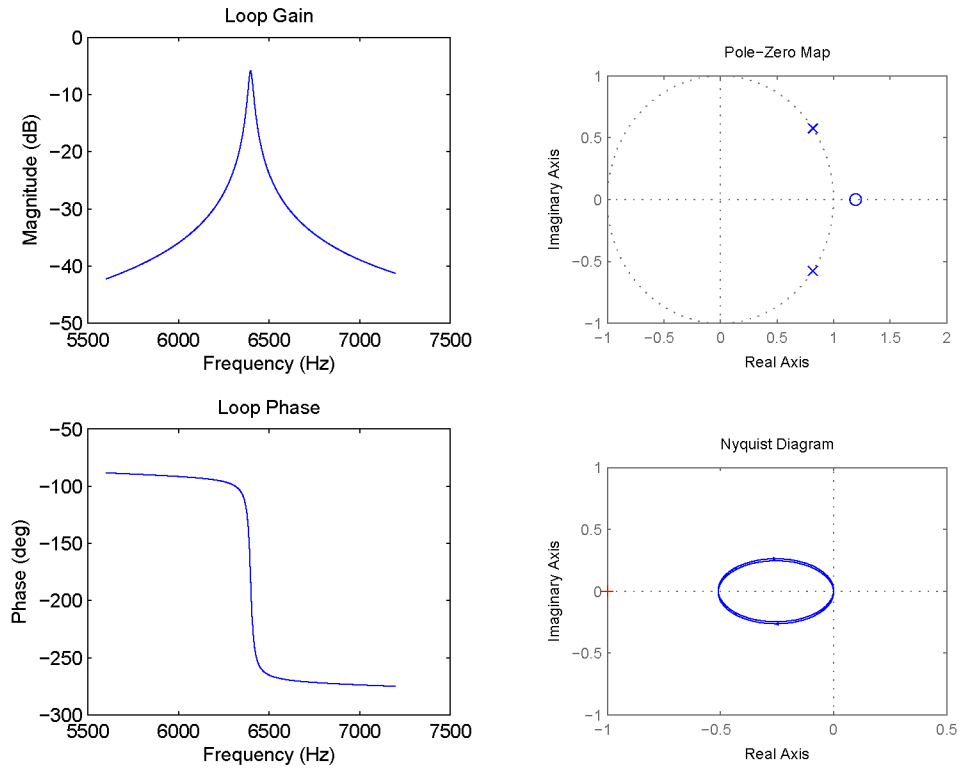


Figure 5.4 Desired loop response of 6 dB gain margin and infinite phase margin.

$$k = \frac{\sqrt{((1 - e^{-\sigma T})\cos(2w_r T) + e^{-2\sigma T} - e^{-\sigma T})^2 + ((1 - e^{-\sigma T})\sin(2w_r T))^2}}{\text{GM}|G(w_r)|\sqrt{a^2 - 2a\cos(w_r T) + 1}} \quad (5.15)$$

### 5.3 Adaptive Design

This section outlines the implementation of an adaptive control algorithm using the equations derived in the previous section. Adaptive resonant control is most commonly used to update plant model coefficients using the method of least squares (19). The adaptation used in that type of control is vastly different from what is described in this section. The main difference is that the control theory presented in this chapter is dependent on the plant frequency response data and not the plant model. This allows

for the controller to adapt to a changing disturbance rather than adapting to a changing plant. This change in the method of adaptation is also necessary due to the lack of resonant modes in the plant.

By changing the focus of control to the disturbance frequency rather than the plant resonant mode, more direct control of the disturbance noise can be achieved. This is because while a typical resonant controller is capable of damping a resonant mode of the plant, this does not ensure maximum reduction of the disturbance. In fact, if a disturbance is primarily tonal and the dominant tonal frequency does not align with the plant resonant mode, very little noise reduction will occur. For this reason, the adaptation of this controller will depend solely on the frequency of the primary tone of the disturbance.

The adaptation algorithm works by identifying the frequency which corresponds to the loudest part of the disturbance noise. Doing this requires the use of an extra microphone to measure the disturbance noise unchanged by any control action. The microphone used for feedback could not be used because the controller would reduce the noise at one frequency only until the noise level somewhere else in the spectrum was louder by comparison. The adaptation algorithm would then switch the control action to the other frequency only to have the previous frequency's loudness increase again. This would cause the controller to quickly alternate between the two loudest parts of the noise spectrum, achieving very little reduction at either frequency. It is for this reason the feedforward microphone of Fig. 5.3 is needed to acquire the disturbance signal for processing.

### 5.3.1 Implementation

So far this chapter has demonstrated a method for finding a single controller,  $H_{con}$ , at a desired frequency,  $w_r$ , using plant frequency response data obtained at that frequency. This seems like an unnecessary simplification since spectrum analyzers have the ability to

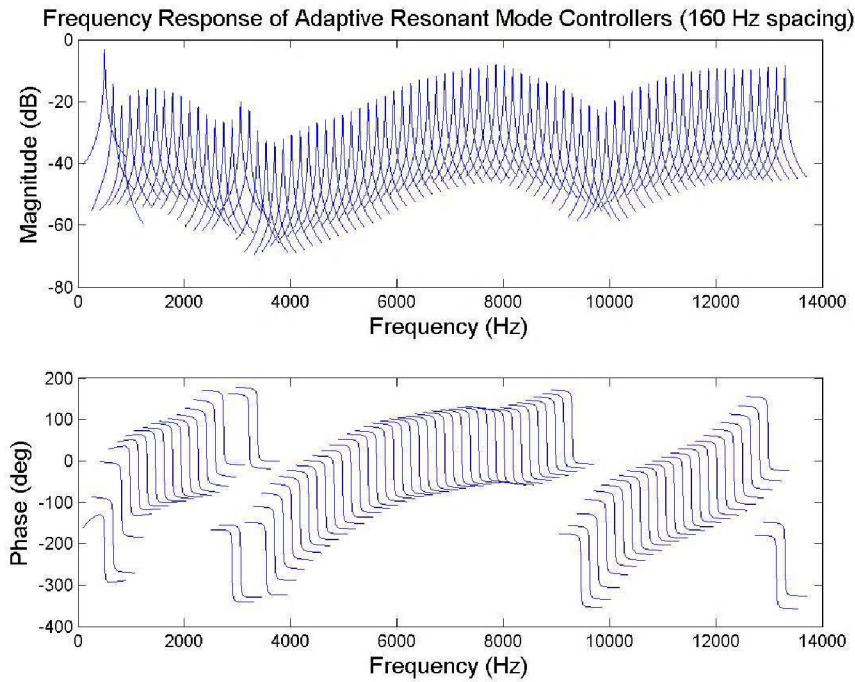


Figure 5.5 Resonant controllers for the headset spanning the entire region of control.

obtain plant frequency response information at many data points across a large frequency range. It is therefore a logical extension to evaluate multiple controllers at multiple data points across the entire frequency range, calculating one controller at each point where plant magnitude and phase data can be experimentally obtained.

The spectrum analyzer used to take plant frequency response data is able to take up to 800 points of data, which means 800 different controllers can be calculated in a single sweep. The frequency response of the headset was obtained from 500-13300 Hz, so a controller could be calculated every 16 Hz using Eq. (5.13)-(5.15). Fig. 5.5 instead shows the controllers calculated at 160 Hz increments across the desired region of control so the reader can more easily see the shape of the resonant modes (the controllers merge together on the figure at 16 Hz spacing).

Now that a good sampling of controllers have been found across the entire region of

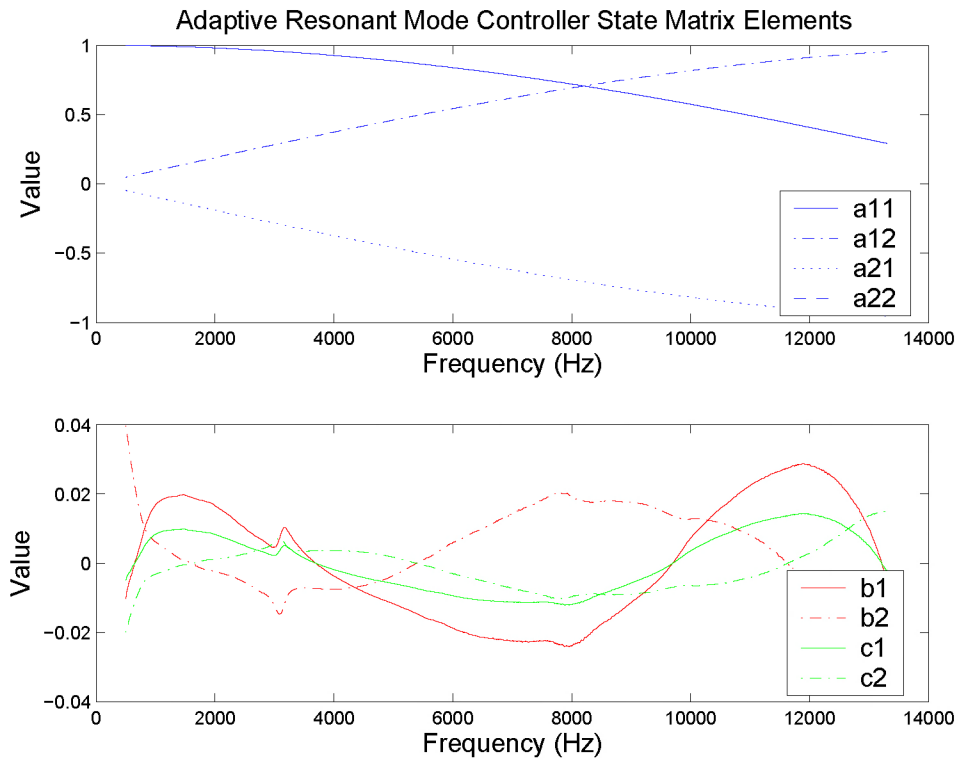


Figure 5.6 Controller matrix elements as a function of frequency.

interest, an adaptive scheme can be implemented which will intelligently switch between controllers based on the disturbance noise. Although the switching algorithm could have just as easily been accomplished by updating transfer function coefficients, a method of updating state-space coefficients was used instead. The modal canonical state-space descriptions of each controller were calculated and are shown as frequency dependent curves in Fig. 5.6. Some manipulation of these matrix elements was necessary to obtain a smooth curve since modal state-space form can yield four different representations from a single controller, as shown in Eq. (5.16). This is because in modal form,  $a_{11} = a_{22}$  and  $a_{12} = -a_{21}$ . Having a smooth curve is very important if linear interpolation between identified frequencies is used in the adaptive algorithm, so using consistent modal matrix form is generally required.

$$\begin{aligned}
H_{con} &= \left[ \begin{array}{cc|c} a_{11} & a_{12} & b_1 \\ a_{21} & a_{22} & b_2 \\ \hline c_1 & c_2 & 0 \end{array} \right] = \left[ \begin{array}{cc|c} a_{11} & a_{12} & -b_1 \\ a_{21} & a_{22} & -b_2 \\ \hline -c_1 & -c_2 & 0 \end{array} \right] \\
&= \left[ \begin{array}{cc|c} a_{11} & a_{12} & -b_2 \\ a_{21} & a_{22} & b_1 \\ \hline -c_2 & c_1 & 0 \end{array} \right] = \left[ \begin{array}{cc|c} a_{11} & a_{12} & b_2 \\ a_{21} & a_{22} & -b_1 \\ \hline c_2 & -c_1 & 0 \end{array} \right] \tag{5.16}
\end{aligned}$$

Implementation of the simulation diagram of Fig. 5.7 allows for real-time updates of the controller state-space matrix elements. This is an input-output description of the adaptive state-space representation of  $H_{con}$  where  $T$  denotes a single sample delay (14). This diagram shows how each discrete input sample from the microphone is manipulated by these values before being output to the speaker. Each element ( $a_{11}, a_{12}, a_{21}, a_{22}, b_1, b_2, c_1, c_2$ ) can be updated as the loudest frequency of the disturbance changes.

### 5.3.2 Results

A Simulink block diagram of the adaptive controller was uploaded onto a real-time I/O board from dSpace. Two 12 bit A/D microphone inputs and one 14 bit D/A speaker output were used. The feedforward microphone input of the disturbance noise was buffered and a 4096 point FFT was performed every 1/16th of a second to determine the frequency of the noise which was the loudest. This provided a  $\pm 8$  Hz resolution for determining  $w_r$ . There is a tradeoff between the number of times in which the controller can be updated and the resolution of the identified frequency. This tradeoff is shown in Table 5.1. If the tonal noise is fairly constant over time, identification of the tonal frequency can be made with a high level of accuracy. However, if the disturbance noise is known to have a quickly varying tonal frequency, lower resolution is to be expected.

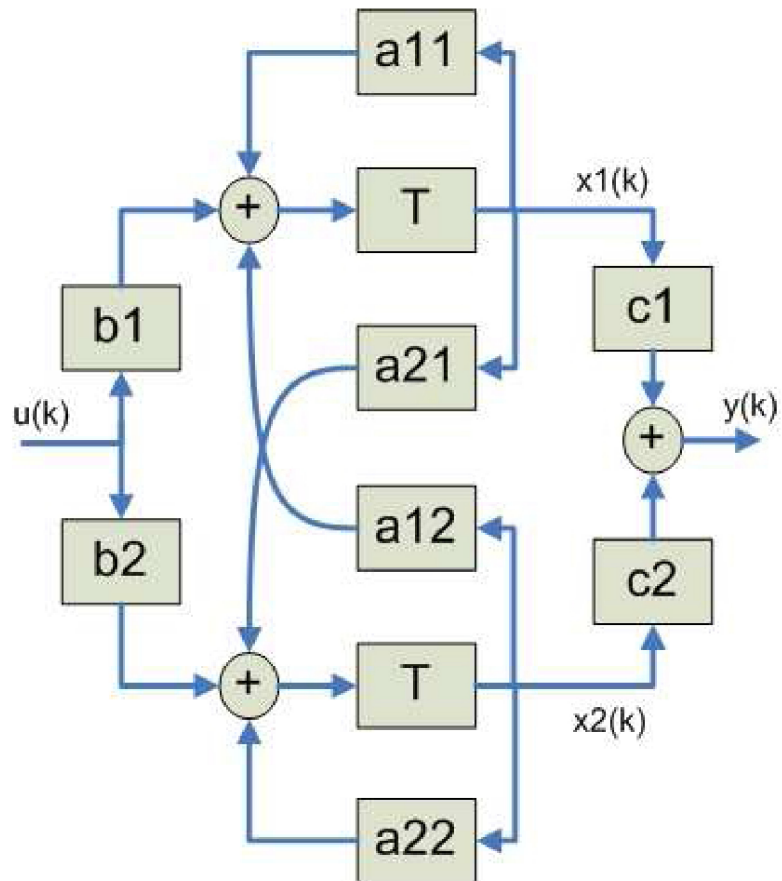


Figure 5.7 Simulation diagram of  $H_{con}$  with adaptive state-space variables.

# of Points	Update Rate	Resolution
1024	1/64 sec	$\pm 32$ Hz
2048	1/32 sec	$\pm 16$ Hz
4096	1/16 sec	$\pm 8$ Hz
8192	1/8 sec	$\pm 4$ Hz
16384	1/4 sec	$\pm 2$ Hz
32768	1/2 sec	$\pm 1$ Hz
65536	1 sec	$\pm 0.5$ Hz

Table 5.1 Trade-off showing the adaptation update rate and the resolution for determining the center frequency of the notch ( $f_s = 65536$  Hz).

The plant magnitude and phase data was obtained from 500-13300 Hz at 16 Hz increments using the spectrum analyzer. This data was used as input to Eq. (5.13)-(5.15) to find the appropriate controllers. A sampling rate of 65536 Hz, a controller shape of  $\sigma = 40$ , and a loop gain margin of 6 dB were chosen as parameters. A high frequency tonal noise source was turned on in front of the dummy head. Fig. 5.8 shows the averaged spectrum of the disturbance before and after control as the frequency of the primary tone of the disturbance varied rapidly from 5800-6000 Hz. The performance of the adaptive controller shows approximately 20 dB of reduction at the primary tone with at most 5 dB increase in noise elsewhere in the spectrum.

## 5.4 Remarks

Miniaturization of the control setup was necessary to overcome the physical restrictions imposed by the headrest design. The headset design was shown to be ideal for controlling high frequency noise because of its close proximity to the ear. A new method for determining resonant mode controllers was presented which allows for direct control of the disturbance. While standard resonant controllers are used for damping fixed resonant poles of the system plant, this new resonant controller is used to create a notch in the disturbance at any frequency. A closed form solution was given which allows for

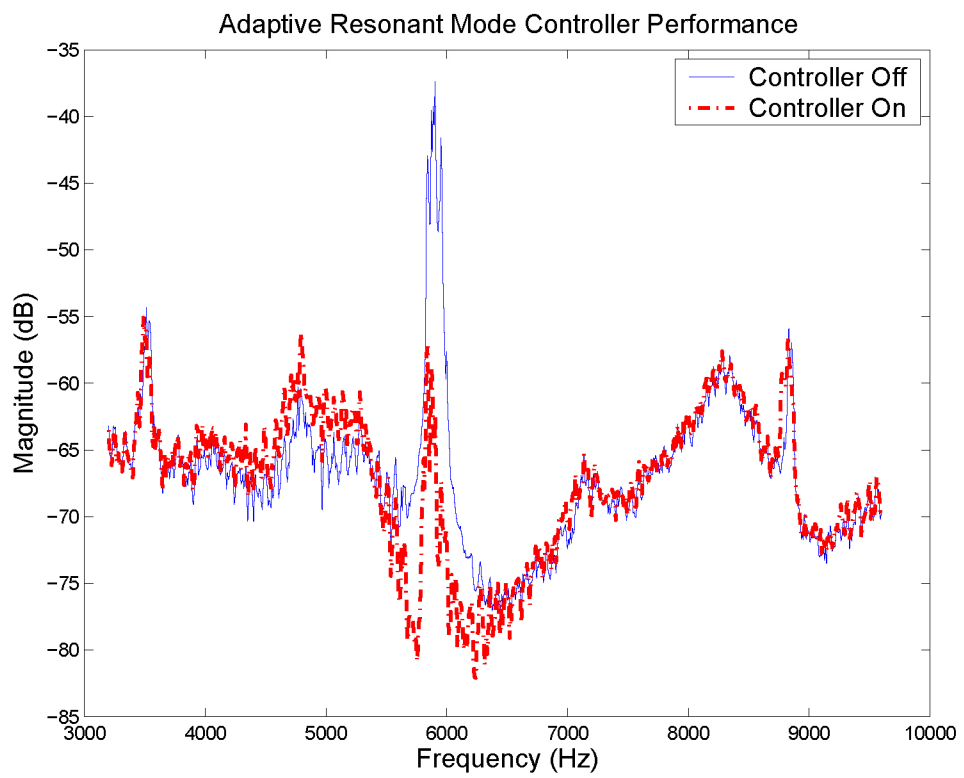


Figure 5.8 Frequency-varying primary tone shows 20 dB of reduction.

the user to specify the gain margin of the resulting loop response. Using the frequency response data of the plant, multiple resonant controllers were identified so the adaptive controller could switch between them based on the loudest disturbance frequency. The experimental results of this adaptive scheme showed large reductions of high frequency tonal disturbances.

## CHAPTER 6. Feedforward Control

The last chapter presented some feedback control strategies to achieve notable narrow-band reductions. An attempt at more broadband active control using the headset system is presented in this chapter using feedforward control. The same microphone used to identify the loudest disturbance frequency for the adaptive controller has the capability of serving a dual purpose as a feedforward microphone in this chapter.

The simplest form of feedforward cancellation consists of a microphone collocated with a speaker so that the transfer function between them can be assumed negligible. A tunable gain inverting amplifier is used to create an anti-noise which cancels the disturbance. This type of feedforward control relies on either an exclusive path between the disturbance and the microphone, an exclusive path between the speaker and the listener, or the fixed locations of the disturbance, speaker, and listener. Also, at high enough frequencies, the distance between the microphone and the speaker is not negligible, and makes feedforward cancellation at these high frequencies impossible. It is these limitations which prevent this type of feedforward action in the headset system.

### 6.1 Band-Limited Plant Inversion

The distance between the feedforward microphone and the speaker (which was assumed negligible at low frequencies) becomes more and more detrimental to control at high frequencies. In order to use feedforward control at high frequencies, the dynamics between the feedforward microphone and the speaker must be identified. Obtaining the

microphone-to-speaker frequency response consisted of using a white noise input through the speaker and sensing it with the microphone in the usual fashion. However, the input and output connections going into the spectrum analyzer were switched so that the result was essentially a microphone-to-speaker response.

Once a microphone-to-speaker response was found, simply negating the complex data yielded a perfect cancellation filter response. Unfortunately, this filter response was unrealizable since the magnitude and phase did not correspond to a stable pole-zero configuration (see Fig. 6.1). This is a common problem with plant inversion based control schemes and cannot be alleviated. Although the entire spectrum cannot be modelled with a realizable filter, certain pieces of the spectrum behave in a manner which can be modelled. These are areas which have a relatively flat magnitude and more importantly, a decreasing phase. Possible candidate regions for this in Fig. 6.1 are the 4000 Hz and 7000 Hz regions. Fitting these sections with a bandpass filter allows for the majority of control action to occur in these sections alone.

As an example, a 1000 Hz bandpass filter is fitted to the frequency response in the 7000 Hz region as seen in Fig. 6.1. The bandpass filter is the feedforward controller which the microphone input signal passes through before it is played through the speaker as a band-limited cancellation noise. This feedforward filter was implemented in real-time using a dSpace controller board. As can be seen in Fig. 6.2, a reduction of 15 dB was achieved over a 1000 Hz range of frequencies. Unfortunately, the noise was increased by 5 dB in other frequency regions. This is due to the bandpass filter not having a steep enough slope to limit the effect of control at other frequencies. This is a hard problem to fix because if the slope was made steeper, the fit to the frequency response data would be worse.

Although the results of Fig. 6.2 are encouraging, the bandpass filter performance was evaluated with the disturbance in a fixed position. Fig. 6.3 shows the required feedforward filter of four more disturbance locations (plotted with the original), each

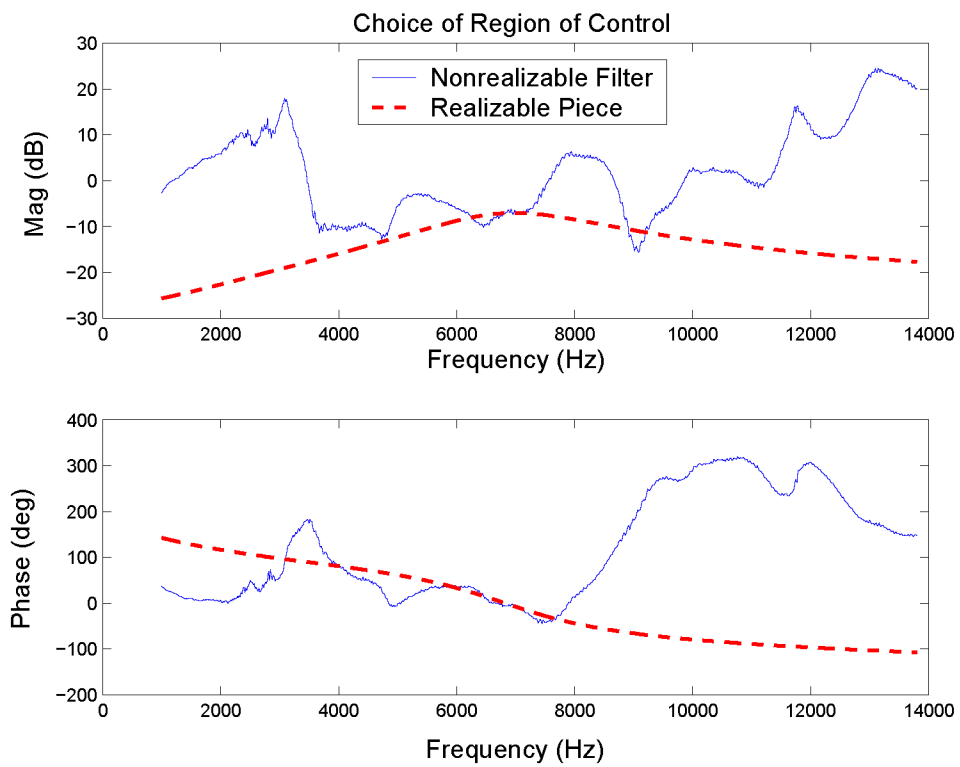


Figure 6.1 A nonrealizable filter is required for perfect feedforward control.

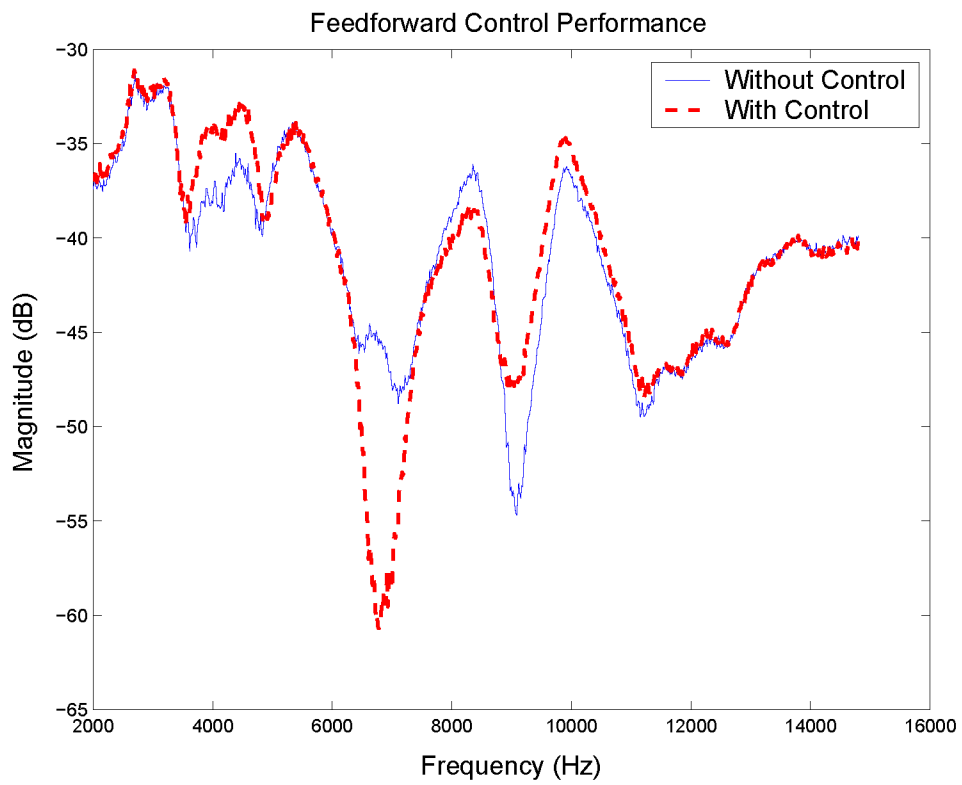


Figure 6.2 Feedforward control performance shows wide-band reductions as well as increases.

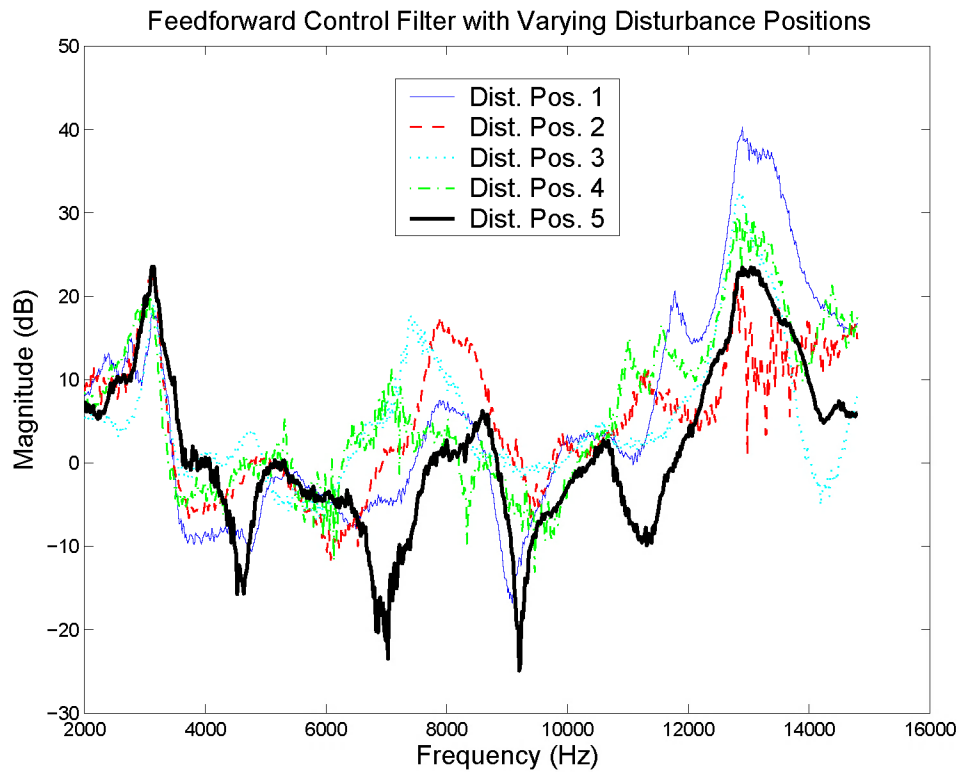


Figure 6.3 Required filter transfer functions for different disturbance positions.

only three inches from the original location. The large variance in the required controller indicates a lack of robustness to disturbance uncertainty. The wide variability of frequency responses is most likely caused by the open-air nature of the headset system. A closed headset which cups around the listener's ear would restrict other noise paths and perhaps reduce this variance. This has not been attempted and will be relegated to future work.

## 6.2 Preview-Based Cancellation

Another promising feedforward design process still in the early stages of testing is a variation of preview-based tracking (21). This method of feedforward control works by previewing the disturbance signal, negating it, performing an fft, multiplying by the

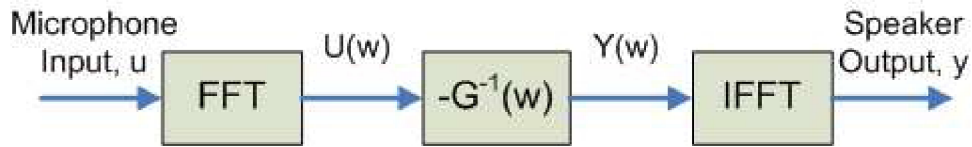


Figure 6.4 Preview-based controller block diagram.

microphone-to-speaker frequency response, then finally outputting the ifft of the result. A block diagram showing this process is given in Fig. 6.4.

An off-line implementation of this control scheme was implemented using a prerecorded three second sample of a tonal disturbance. The 15 dB broadband reductions of Fig. 6.5 are quite impressive, however, the control input was completely determined off-line and the performance should be viewed as the best-case of this type of feedforward control. Experiments executed in real-time do not expect to perform this well because of the large number of samples required to perform the fft/ift coupled with the very short transport delay from microphone to speaker. Future work with real-time testing will determine the feasibility of preview-based feedforward control.

### 6.3 Remarks

It was determined that the physical distance between sensor and actuator could not be made small enough to be considered negligible when controlling high frequency noise. This eliminated the possibility of a feedforward scheme which would simply negate the input disturbance. By identifying the dynamics between the sensor and actuator, a nonrealizable filter response could be obtained and a bandpass filter could be fit to the realizable portions. This band-limited inversion technique achieved large reductions over a fairly wide frequency range but was not robust to changes in the disturbance location. Finally, a preview-based feedforward control scheme accomplished large broadband reductions in an off-line experiment. Future work with real-time testing

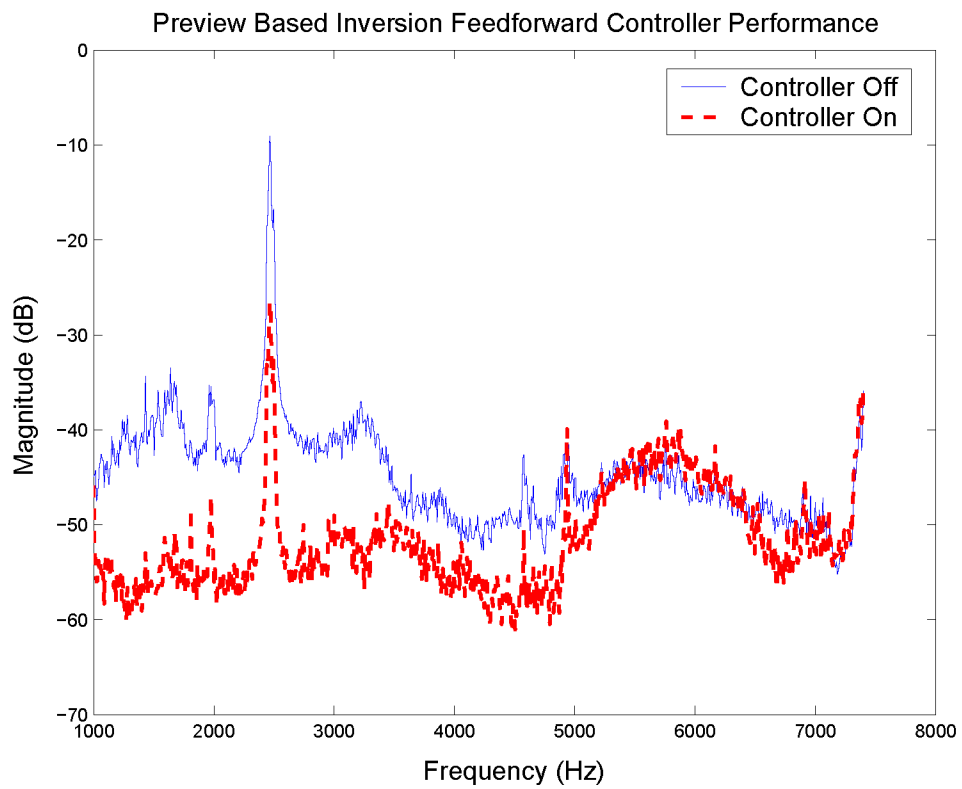


Figure 6.5 Preview-based feedforward performance with control input signal determined off-line.

will determine the true capabilities of this method.

## CHAPTER 7. Conclusions and Future Work

This chapter is aimed at summarizing the research findings and presenting some directions for future research. Chapter 2 described the code development efforts aimed at expanding the functionality of the SOCIT system identification software. The first code developed preconditions the input data to ensure a highly accurate discrete-time model at any sampling rate. The second code developed flips and shifts the input data and modulates the transfer function output to obtain accurate models in any frequency band. Although the resulting system transfer function is changed, these codes do not alter the SOCIT algorithm directly. Future work could incorporate these two codes into SOCIT in a user-friendly manner. A more challenging task would be to rewrite the SOCIT code from within to account for these modifications. Improvements can also be made when finding the best  $f_s$  ratio and gain shift parameters needed to generate the most accurate models. The current method uses an exhaustive search which takes considerable time. Future work could address mathematical derivation of the optimal gain shift and  $f_s$  ratio parameters.

A simple automated synthesis procedure was introduced in Chapter 3 which yields state weights and corresponding controller gains with excellent performance. This method significantly reduces the time typically required for the LQG controller design process using a trial and error method. This is especially useful for very high order controllers specific to many acoustic and vibration problems. Further analysis of this synthesis procedure could be done using higher order system models as well as MIMO models to test any limitations which may arise. A comparison of this automated syn-

thesis method with genetic algorithms, neural networks, and other known optimization methods would also be of interest.

Chapter 4 introduced an in-seat active noise control setup used for controlling high frequency noise. An alternative method of resonant mode control was proposed to exert some control authority to a narrow frequency band. This alternative method of control succeeded in creating a notch filter effect on a disturbance noise at any desired frequency. Future work could analyze the performance and robustness characteristics involved with changing the control bandwidth by increasing the order of the controller. Future work could also attempt to increase the region of silence surrounding the error microphone by using multiple sensors or a different control scheme.

The control setup in chapter 5 used very small speakers and microphones in close proximity to a listener's ear. Using this configuration, an adaptive resonant mode controller was implemented which was able to significantly reduce a frequency varying tonal disturbance. Future work should attempt multiple tone control of the next highest tones of the disturbance. The controller presented in this chapter also assumes a fairly flat plant frequency response. More work could be done to determine when this assumption is reasonable and when it breaks down.

Finally, chapter 6 explored several possible feedforward control designs. It was determined that complete cancellation could only occur with the use of an unrealizable filter. Future work could involve changing the speaker and microphone orientations such that the shape of the generally unstable microphone-to-speaker frequency response could be more easily modeled as a stable transfer function over a desired frequency band. Also, a preview-based feedforward controller is implemented off-line with promising results. Future work should address implementation of this methodology in real-time experiments.

## BIBLIOGRAPHY

- [1] Barton, C.K., Mixson, J.S., “Noise Transmission and Control for a Light Twin-Engine Aircraft.” *Journal of Aircraft*, Vol. 18, No. 7, 1981.
- [2] Bies, David A., Hansen, Colin H., *Engineering Noise Control: Theory and Practice, 2nd Edition*. Spon Press, New York, New York 1996.
- [3] Palumbo, Dan, Cabell, Ran, Cline, John, Sullivan, Brenda, “Active Structural Acoustic Control of Interior Noise on a Raytheon 1900D.” NASA Langley Technical Report, 2000.
- [4] Chen, Chi-Tsong, *Linear System Theory and Design, 3rd Edition*. Oxford University Press, New York, New York 1999.
- [5] Franklin, Gene F., Powell, J. David, Emami-Naeini, Abbas, *Feedback Control of Dynamic Systems, 4th Edition*. Prentice Hall, Upper Saddle River, New Jersey 2002.
- [6] Grewal, A., Nitzsche, F., Zimcik, D.G., Leigh, B., “Active Control of Aircraft Cabin Noise Using Collocated Structural Actuators and Sensors.” *Journal of Aircraft*, Vol. 35, No. 2, 1998.
- [7] “HMS II HEAD Measurement System Manual.” HEAD acoustics GmbH, 1995.
- [8] Juang, Jer-Nan, *Applied System Identification*. Prentice Hall Inc., Englewood Cliffs, New Jersey 1994.

- [9] Kestell, Colin D., Cazzolato, Ben S., Hansen, Colin H., “Active Noise Control in a Free Field with Virtual Sensors.” Acoustical Society of America, 2001.
- [10] Lathi, B.P., *Signal Processing and Linear Systems*. Berkeley-Cambridge Press, Carmichael, California 1998.
- [11] Lathi, B.P., *Modern Digital and Analog Communication Systems, Third Edition*. Oxford University Press, New York, New York 1998.
- [12] Lewis, Frank L., Syrmos, Vassilis L., *Optimal Control, 2nd Edition*. John Wiley and Sons Inc., New York, New York 1995.
- [13] Liu, Feng, “Active Feedback Control of Acoustic Noise in 3-D Enclosures.” Masters Thesis, Iowa State University, 2002.
- [14] Phillips, Charles L., Nagle, H. Troy, *Digital Control System Analysis and Design, Third Edition*. Prentice Hall Inc., Upper Saddle River, New Jersey 1995.
- [15] Pota, H.R., Moheimani, S.O. Reza, Smith, Matthew, “Resonant Controllers for Flexible Structures.” IEEE Proceedings of the 38th Conference on Decision and Control, Phoenix, Arizona, December 1999.
- [16] Rafaely, B., Elliot, S.J., Garcia-Bonito, J., “Broadband Performance of an Active Headrest.” Acoustical Society of America, 1999.
- [17] Rafaely, Boaz, Elliot, Stephen J., “ $H_2/H_\infty$  Active Control of Sound in a Headset: Design and Implementation.” IEEE Transactions on Control Systems Technology, Vol. 7, No. 1, January 1999.
- [18] Skogestad, Sigurd, Postlethwaite, Ian, *Multivariable Feedback Control*. John Wiley and Sons Inc., West Sussex, England 1996.

- [19] Tjahyadi, Hendra, He, Fangpo, Sammut, Karl, "Vibration Control of a Cantilever Beam Using Adaptive Resonant Control." 5th Asian Control Conference, Vol. 3, July 2004.
- [20] Vaicaitis, R., Mixson, J.S., "Theoretical Design of Acoustic Treatment for Noise Control in a Turboprop Aircraft." Journal of Aircraft, Vol. 22, No. 4, 1985.
- [21] Zou, Qingze, "Preview-based System-Inversion for Output Tracking: Theory and Practice." PhD Thesis, University of Washington, 2003.